AMERICAN UNIVERSITY OF BEIRUT

MORPHOLOGICAL STUDY OF TRICHOPLAX ADHAERENS USING A PHASE FIELD MODEL

by
ASHOD KARKOUR KHEDERLARIAN

A thesis
submitted in partial fulfillment of the requirements
for the degree of Master of Science
to the Department of Physics
of the Faculty of Arts and Sciences
at the American University of Beirut

Beirut, Lebanon
May 2021

AMERICAN UNIVERSITY OF BEIRUT

Morphological Study of Trichoplax Adhaerens Using a Phase Field Model

by

Ashod Karkour Khederlarian

Approved by: 29 April 2021

Dr. Sara Najem, Assistant Professor — Advisor

Physics

LKlushin 29 April 2021

Dr. Leonid Klushin, Professor — Member of Committee

Physics

29 April 2021

Dr. Martin Grant, Professor — Member of Committee

Physics, Mcgill University

Date of thesis defense: April 28, 2021

AMERICAN UNIVERSITY OF BEIRUT

THESIS, DISSERTATION, PROJECT RELEASE FORM

Student Name:	Khederlarian	Ashod	Karkour
	Last	First	Middle

☑ Master's Thesis ○ Master's Project ○ Doctoral Dissertation

☑ I authorize the American University of Beirut to: (a) reproduce hard or electronic copies of my thesis, dissertation, or project; (b) include such copies in the archives and digital repositories of the University; and (c) make freely available such copies to third parties for research or educational purposes.

☐ I authorize the American University of Beirut, to: (a) reproduce hard or electronic copies of it; (b) include such copies in the archives and digital repositories of the University; and (c) make freely available such copies to third parties for research or educational purposes after: **One ___ year from the date of submission of my thesis, dissertation or project.**
Two ___ years from the date of submission of my thesis , dissertation or project.
Three ___ years from the date of submission of my thesis , dissertation or project.

Signature

May 6, 2021

Date

This form is signed when submitting the thesis, dissertation, or project to the University Libraries

Acknowledgements

First I would like to thank my advisor Professor Sara Najem for all her guidance and support. Our many meetings have always helped me keep a steady pace and guided me out of many valleys during exploration. I would also like to thank the committee members Professor Leonid Klushin and Professor Martin Grant for their constant feedback and help. They were always present when I reached out.

In addition, I would like to thank my colleagues and peers. The seniors: Carmen Al Masri, Kafa Alameh, Rodrique Badr, Ahmad Lalti, and Wassim Sleiman, have all acted as older siblings guiding me through my first years at AUB. Those who started with me: Ibrahim Nourredine, Hassan Taki, and Sahag bozoian, have all helped in sharing common burdens. Everyone contributed in their own way to a very vibrant and friendly graduate room, which helped us all through difficult times.

All of this would not be possible if not for the resilience and dedication of all my grandparents, who have settled in Lebanon in one way or the other, and have worked extremely hard to make sure future generations have a better quality of life.

Above all, I would like to thank my parents for their unconditional love and support. They have always let me steer my way through life, patting me on my back when I succeed, and lifting me up when I fail.

An Abstract of the Thesis of

Ashod Karkour Khederlarian for Master of Science
Major: Physics

Title: Morphological Study of Trichoplax Adhearens Using a Phase Field Model

Understanding the physics of free boundary dynamics and the kinetics of non-equilibrium phase transformation was, and still is, essential to the advancement of technology in terms of engineered materials. Even historically, said physics was paramount during the industrial revolution because it facilitated the wide-scale production of steel and other alloys. It did so because, at the critical points of solidification and precipitation, dynamical free boundaries are formed, which are often described by sharp interface models (e.g., the Stefan problem).

Despite current advances in computational physics, such models are difficult to solve, even numerically. A more convenient model is a phase-field one, where the interface is taken to be continuous rather than sharp. Mathematically, this is achieved by introducing a field (order parameter), which assumes a constant value in the bulk of each phase and varies continuously along the interface. One then solves for this field, among others (temperature, strain, etc.), by writing a free energy functional and minimizing it. The advantages this model provide are illustrated in its application to the Grinfeld instability, where stress-induced forces cause an instability at the interface between a uni-axially strained solid and its melt. Naturally, this model is attractive when thinking about biological systems because they can be thought of as materials with a free boundary and elastic properties.

In this thesis, we propose to apply this model to study the dynamic morphology of a peculiar little creature known as Trichoplax adhaerens (Placozoa). It has a thin flat body composed of a few thousand cells of six types, and it moves using cilia on its external surface. To do so, we numerically model its dynamics as a 2D conserved phase field coupled to an elastic field and subject to a time dependent external forcing. The behavior of an initial random surface is analyzed for a linear and power-law decreasing dependence. This analysis is quantified by introducing the structure factor S(q), defined as the Fourier transform of the

height-height correlation function. Initial profiles of different Fourier modes are also analyzed similarly. We find that the power-law dependence is much better in mimicking the out-of-plane buckling observed in the creature. Lastly, we also extend the model to 3D, but only briefly explore it due to time constraints.

Contents

List of Figures

Chapter 1

Motivation

Moving boundary problems are abundant when studying dynamical systems ranging from the biological to the physical. Often these problems are formulated with partial differential equations (PDEs) alongside boundary conditions imposed on an evolving interface (eg. the generalized Stefan problem [1]). Solving such problems computationally can be quite challenging, mainly due to the need of explicitly tracking the boundary.

The phase field method [2] offers an alternative approach by introducing a new dynamical field ϕ which acts as a marker for different phases and which varies continuously from one phase to the other. Having its origins in critical phenomena [3], the term "phase" typically refers to the familiar notion of phases in physics (e.g. a solid and its melt). However, specially in biological applications, it should be understood in a much more broader sense [1]. Typically, ϕ is coupled to other fields, such as temperature, through a Ginzburg-Landau free energy, the minimization of which results in a set of PDEs for the fields which can be solved numerically, even in 3D [4].

The main appeal of the method stems from the fact that the boundary between the phases is tracked implicitly by the phase field itself, thus eliminating the need for explicit boundary tracking. It has been successfully implemented on a range of physical problems, such as dendrite growth, Grinfeld instability, and spinodal decomposition [5–8], and a range of biological problems, such as cell migration, neural growth, and immune response [9–11]. Apart from this advantage, the model is also favorable in some of the cases mentioned because of how easily it incorporates surface tension as an energy cost for interfaces.

As mentioned above, besides the phase-field, there can be other fields which greatly influence the morphological dynamics of materials and phase transformations, such as temperature and elasticity. One example of interest is Grinfeld Instability, which refers to an instability at the surface of a uniaxially strained solid in contact with its melt. In short, the instability is due to a feedback loop

[1] When modeling a cell, one phase can be 'inside the cell' and the other 'outside the cell'.

of stress-relief and groove formation. Valleys on the surface will be more stressed than hills, which can be relieved via surface diffusion from valleys to hills, or through phase change. These, in turn, cause valleys to grow further, increasing the stress gradient and causing more diffusion/phase change. This phenomenon has all the ingredients necessary for phase-field modeling, and indeed Muller and Grant [6] have analyzed it using a phase-field coupled to an elastic field. Evidently, similar effects due to elasticity are common in amorphous living creatures with dynamic boundaries, suggesting some mapping with the Grinfeld problem. However, the model suggested above can not immediately be applied on living beings for 2 main reasons: 1) The dynamics of organisms is conserved[2] 2) any sort of buckling instability is not really unstable in the sense of indefinite growth[3]. We solve these issues by firstly modeling the phase field such that it is conserved, and secondly by limiting the unstable growth through a time-dependent external stress. The latter can be done in many ways; we explore the dynamics resulting from a linear and power-law dependence.

The main motivation in doing so is the morphological dynamics of trichoplax adhaerens, a flat multi-cellular organism in the phylum Placozoa [12]. Due to a lack of sensory and muscle cells, it exhibits nearly random movements, which result in some strange dynamics, namely out-of plane buckling and subsequent relaxation. We run numerical simulations in two and three dimensions, and recover characteristic time and length scales of buckling and subsequent relaxation.

[2]Ultimately it is not really conserved because of eating food and using energy, but it definitely is conserved within the time scales of modeling.

[3]In Grinfeld instability, a corrugation on the surface of a metal grows without bounds, as long as it is far from the boundaries of the system.

Chapter 2

Introduction

In this chapter, we start by laying the foundations and general notions upon which discussions of out of equilibrium thermodynamics stand in section 2.1. Then, in section 2.2, we move to a particular model of out of equilibrium dynamics, which is the phase field model, starting with some historical background and then providing examples of conserved and non-conserved dynamics. Afterwards, we introduce the theory of elasticity in section 2.3. This is followed by section 2.4, where we formulate the Grinfeld instability problem before phase field modeling, and show that it can also be formulated using a phase field coupled to an elastic field. Finally, we end in section 2.5 with how all of this ties to the initial motivation: Trichoplax adhaerens.

2.1 Out of Equilibrium Dynamics

Out of equilibrium systems are analyzed as coarse-grained systems, made up of small mesoscopic counterparts which are assumed to be at local equilibrium[1] [13]. Under this assumption, equilibrium thermodynamic variables such as entropy, energy, and temperature can be used to define the system, given that they are functions of time and position, and that common thermodynamic relations are true only locally. These subsystems are not at equilibrium with each other, and so the system as a whole is not in global equilibrium, allowing for fluxes of different quantities between them. These fluxes in turn dictate the rates of change of the quantities by the continuity equation

$$\frac{\partial c_i}{\partial t} = -\vec{\boldsymbol{\nabla}} \cdot \vec{\boldsymbol{J}}_{\boldsymbol{i}} + \dot{\rho}_i, \tag{2.1}$$

where c_i is a scalar field (such as concentration), $\vec{\boldsymbol{J}}_{\boldsymbol{i}}$ is its flux, and $\dot{\rho}_i$ is the rate of production, which is zero if there are no sources or sinks. The fluxes are deter-

[1] the assumption of local equilibrium is based upon two characteristic time scales: the relaxation time of the mesoscopic subsystems, and the relaxation time of the system as a whole. If the latter is much greater than the former, then the system is said to be in local equilibrium.

mined by thermodynamic forces, which are generally gradients of thermodynamic potentials[2]. Some well known examples are Fourier's Law and Fick's Law

$$\vec{\boldsymbol{J_Q}} = -K\vec{\boldsymbol{\nabla}}T, \tag{2.2}$$

$$\vec{\boldsymbol{J_i}} = -M\vec{\boldsymbol{\nabla}}\mu_i, \tag{2.3}$$

where T is the temperature that can be regarded as the potential for heat flow, and μ is the chemical potential. It should be also noted that the potentials themselves can be obtained through thermodynamic relations (e.g. $\mu = \frac{\partial F}{\partial N}$).

It should be clear by now that fluxes and forces are explained through a phenomenological theory expressing the intricate relations between different thermodynamic conjugate variables [14]. As an example, take the conjugate pair concentration/chemical potential. The chemical potential is defined as the partial derivative of the free energy with respect to concentration. In turn, the gradient of this potential is the force that drives the flux of concentration. Finally, the time evolution of concentration is proportional to this flux through equation 6.

The dynamics of order parameter fields (introduced below) are treated by exact analogy. However, these fields can be either conserved or non conserved.

2.2 Phase-Field Model

2.2.1 Order Parameters

Historically, order parameters were first introduced by Lev Landau [15] to explain second order phase transitions, where state variables such as energy (obtained as first derivatives of the free energy) change continuously from one phase to the other, while second derivatives (susceptibilities) change discontinuously. The order parameter described a type of order in the system, for example magnetization in the context of paramagnetic-ferromagnetic phase transformation. Landau treated the order parameter as a state variable itself, which takes on one value in the bulk of one phase and another value in the bulk of the other phase. Such a treatment permits one to express the thermodynamic potential of the system as a function of the order parameter ϕ, among other state variables depending on the chosen ensemble (e.g. temperature and volume)

$$F = F(V, T, \phi). \tag{2.4}$$

This potential can be expanded in a Taylor series around the transition point:

$$F(V, T, \phi) = F_0 + c1\phi + c2\phi^2 + c3\phi^3 + O(\phi^4), \tag{2.5}$$

[2]This is analogous to classical mechanics, where the force on a particle in a potential is proportional to the gradient of that potential. This ensures that the force which pushes on the particle (causing a 'flux') is such that at equilibrium the potential energy is minimized.

where F_0 is the potential at the transition point, and the coefficients of expansion depend on temperature and volume. One can obtain the order parameter at equilibrium by the condition

$$\left.\frac{\partial F}{\partial \phi}\right|_{T,V} = 0. \tag{2.6}$$

Such a model allows only the study of bulk thermodynamics, where phases are assumed to be infinite in extent and uniform. For a more general analysis, which takes into account the finiteness of the phase, multiple coexisting phases, and even the interface separating them, the state variables are considered as functions of position. Then, it is possible to define a free energy density, and the free energy as an integral over space of this density

$$F = \int_V f(\phi(\vec{\boldsymbol{r}}), T(\vec{\boldsymbol{r}}))d^3\vec{\boldsymbol{r}}. \tag{2.7}$$

However, when studying dynamics out of equilibrium, and in particular coexisting phases, such a functional can lead to unphysical systems composed of many sharp boundaries separating many phases. That is because equation 4 does not incorporate interfacial energy, which was later added by Cahn and Hilliard [16] [17].

$$F = \int_V \left[f_{bulk}(\phi(\vec{\boldsymbol{r}}), T(\vec{\boldsymbol{r}})) + \frac{1}{2}|W_0 \boldsymbol{\nabla}\phi|^2 \right] d^3\vec{\boldsymbol{r}}. \tag{2.8}$$

In the language of order parameters, interfaces take on the meaning of large gradients in the parameter, and so adding this term acts as a penalty for them, preventing instabilities solely by the fact that the system wants to reduce the free energy. W_0 is a parameter of units $[J/m]^{\frac{1}{2}}$ related to surface tension.

The order parameter itself can either be conserved or non-conserved, leading to different dynamics labeled Model B and A, respectively.

2.2.2 Model B: Conserved Field

As discussed above, the dynamics of a conserved order parameter field (known as model B in the literature [3]) can be obtained by first defining the chemical potential as a variational derivative of the free energy, since the latter is a functional of the order parameter (eq. 2.8)

$$\mu = \frac{\delta F[\phi]}{\delta \phi}. \tag{2.9}$$

The gradient of this potential gives the thermodynamic "force", which generates the flux:

$$\vec{\boldsymbol{J}} = -M\vec{\boldsymbol{\nabla}}\mu, \tag{2.10}$$

where M is known as the mobility. The negative sign is there to ensure that fluxes are directed from high potential to low potential. Finally, the rate of change of the order parameter field is given by the continuity equation

$$\frac{\partial \phi}{\partial t} = -\vec{\boldsymbol{\nabla}} \cdot \vec{\boldsymbol{J}}. \tag{2.11}$$

It should be noted that this is only the flux due to thermodynamics, which tries to minimize the free energy. Other kinetic terms should be added as other fluxes, as is done in [10], where a neutrophil was modeled as a phase field chasing a parasite. In that case, there are two fluxes entering equation 11. One is of thermodynamic origin, and it is due to the neutrophil itself ($\vec{\boldsymbol{J}}_1 = -M\vec{\boldsymbol{\nabla}}\mu$), and the other is due to the fact that the neutrophil wants to chase the parasite with a velocity V ($\vec{\boldsymbol{J}}_2 = \phi\vec{\boldsymbol{V}}$) generated from chemical cues.

An example of model B dynamics is spinodal decomposition below a critical temperature, where a mixture of two species separates into domains where only one species is present. In this situation, the Landau free energy expansion takes on the following form:

$$f(\phi) = a(T) + \frac{a_2(T)}{2}\phi^2 + \frac{a_4(T)}{4}\phi^4 + O(\phi^6), \tag{2.12}$$

where the order parameter ϕ takes on the meaning of concentration of one species relative to its initial homogeneous concentration, and the expansion is done around the critical temperature, so T is actually $T - Tc$. Odd terms are omitted because the free energy is symmetric in the two states corresponding to the two species, e.g. $f(\phi) = f(-\phi)$. $a(T)$ corresponds to the free energy at the critical point (which does not matter because it vanishes when taking derivatives), and $a_2(T)$ along with $a_4(T)$ determine the potential of ϕ, the minima of which correspond to stable equilibrium states. Above the critical temperature, $T > T_c$, $a_2(T) > 0$ and $a_4(T) > 0$, which corresponds to only a single minimum at $\phi = 0$. Below the critical temperature, $T < T_c$, $a_2(T) < 0$ and $a_4(T) > 0$, which corresponds to two symmetric minima (figure 2.1).

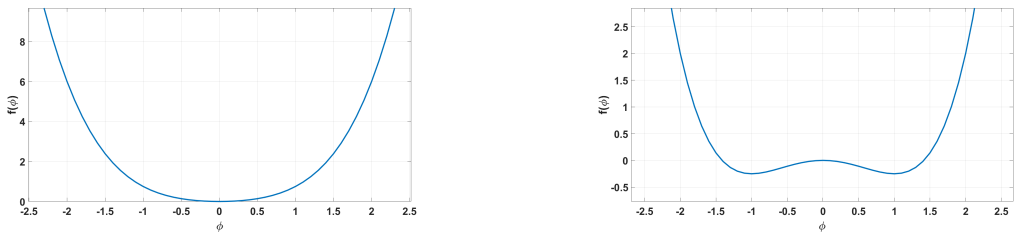

(a) $f(\phi) = \frac{\phi^2}{2} + \frac{\phi^4}{4}$. (b) $f(\phi) = -\frac{\phi^2}{2} + \frac{\phi^4}{4}$.

Figure 2.1: The landau free energy expansion for a) $T > T_c$ and b) $T < T_c$.

With this free energy density, the equation of motion for ϕ (eq. 2.11) becomes

$$\frac{\partial \phi}{\partial t} = M\nabla^2(-W_0\nabla^2\phi + a_2\phi + a_4\phi^3). \tag{2.13}$$

For $a_2 = -1$ and $a_4 = 1$, an initial homogeneous configuration with $\langle\phi\rangle = 0$ becomes unstable. This can be simulated by initiating the phase-field as a random variable on each grid point obtained from a Gaussian distribution of average zero and standard deviation 0.001 (figure 2.2).

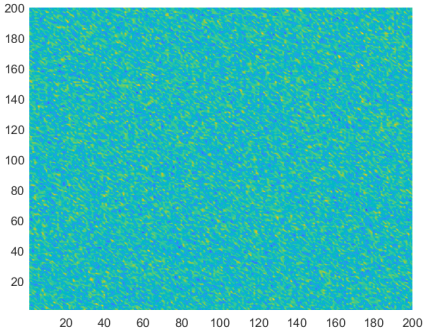

(a) The phase field at $t = 0$, where each grid point is a random variable sampled from a Gaussian of average 0 and standard deviation 0.001.

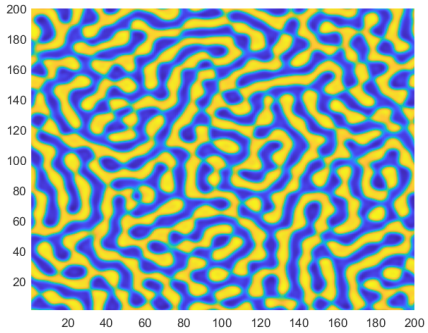

(b) The phase field at $t = 3$. Different domains of $\phi = 1$ and $\phi = -1$ start appearing.

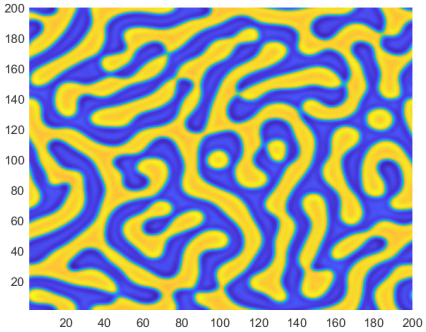

(c) The phase field at $t = 10$. The domains are well separated with clear boundaries between them.

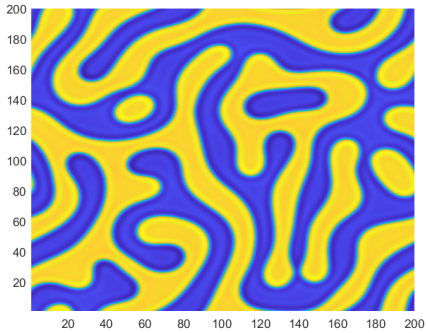

(d) The phase field at $t = 40$. The different domains keep growing and eventually connect. The dynamics here is slower.

Figure 2.2: Spinodal decomposition of an initial mixture of two species. Here the order parameter is the concentration of one species relative to the initial homogeneous concentration. $M = W_0 = 1$. Yellow corresponds to $\phi = 1$ and blue corresponds to $\phi = -1$. Coarsening is clearly observed, albeit it slows down with time.

2.2.3 Model A: Nonconserved Field

For nonconserved fields (known as model A), one needs not to worry about fluxes in order to ensure local conservation of the field. Therefore, the simplest dynamics is due to the variational derivative itself, which is the force that drives the dynamics towards equilibrium, given by:

$$\frac{\partial \phi}{\partial t} = -M \frac{\delta F[\phi]}{\delta \phi}. \tag{2.14}$$

This ensures that locally ϕ changes in such a manner as to reduce the overall free energy, eventually reaching equilibrium, where the field doesn't evolve anymore since $\frac{\delta F[\phi]}{\delta \phi}\Big|_{eq} = 0$. An example of model A dynamics is magnetic domain growth below a critical temperature, where a homogeneous state of zero average magnetization becomes unstable. In this case, the same free energy of equation 2.12 can be used, but now ϕ is the magnetization of the system, and the odd terms are zero because the system is symmetric under a 180° rotation. The equation of motion becomes

$$\frac{\partial \phi}{\partial t} = M(W_0 \nabla^2 \phi - a_2 \phi - a_4 \phi^3). \tag{2.15}$$

For $a_2 = -1$ and $a_4 = 1$, an initial homogeneous configuration with $\langle \phi \rangle = 0$ becomes unstable. This can be simulated by initiating the phase-field as a random variable on each grid point obtained from a Gaussian distribution of average zero and standard deviation 0.001 (figure 2.3).

Both models do not include effects due to stresses and strains, unless a relevant term is added to the bulk free energy. Such a term, along with its implications and meaning, is introduced in the next section.

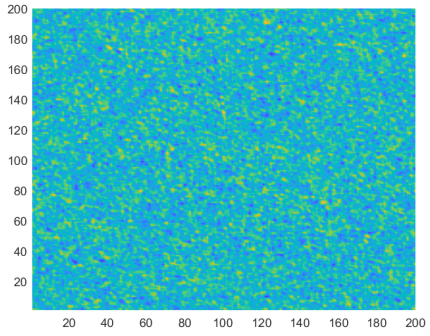

(a) The phase field at $t = 0$, where each grid point is a random variable sampled from a Gaussian of average 0 and standard deviation 0.001.

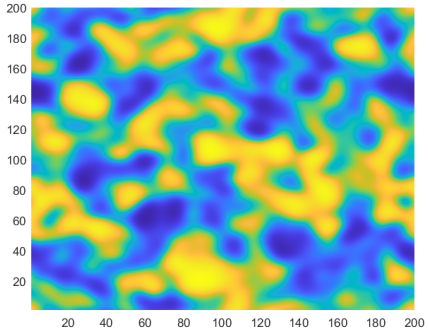

(b) The phase field at $t = 3$. Different domains of $\phi = 1$ and $\phi = -1$ start appearing.

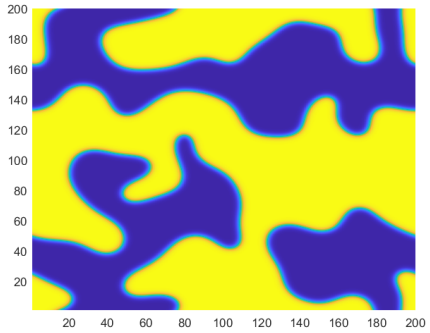

(c) The phase field at $t = 10$. The domains are well separated with clear boundaries between them.

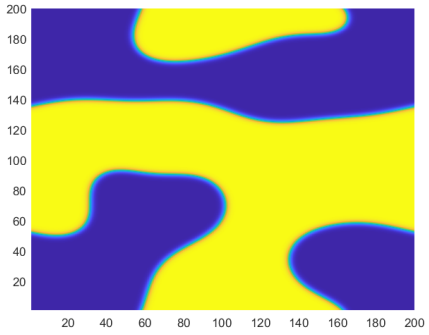

(d) The phase field at $t = 40$. The different domains keep growing and eventually connect. The dynamics here is slower.

Figure 2.3: The evolution of an initial field of zero average magnetization with seeds on a 200x200 grid with periodic boundary conditions. $M = W_0 = 1$. Yellow corresponds to $\phi = 1$ and blue corresponds to $\phi = -1$.

2.3 Elasticity

2.3.1 Deforming a Continuous Body

When a body is deformed, for whatever reason, all parts of the system get displaced by a certain amount. The body is treated as a continuous medium, with x_i (i ranging from 1 to 3 in 3 dimensions) being the position of a point in the body. Let the position of this same point be x_i' after the deformation. It follows by definition that the displacement of this point is given by a vector $\vec{\boldsymbol{u}}$

with components:

$$u_i = x'_i - x_i, \tag{2.16}$$

which is called a displacement vector.

Now consider two points infinitesimally close to each other, separated by a distance $dl^2 = dx_1^2 + dx_2^2 + dx_3^2$. After a deformation, the new separation along each direction is $dx'_i = dx_i + du_i$, and so the new distance between the points becomes:

$$dl'^2 = (dx_i + du_i)^2 = dl^2 + 2\frac{\partial u_i}{\partial x_k}dx_i dx_k + \frac{\partial u_i}{\partial x_k}\frac{\partial u_i}{\partial x_l}dx_k dx_l, \tag{2.17}$$

where the chain rule has been used for du_i, and repeated indices are summed over (Einstein summation convention). The second term can be equally written in a symmetric form $\big(\frac{\partial u_i}{\partial x_k} + \frac{\partial u_k}{\partial x_i}\big)dx_i dx_k$, which leads to

$$dl'^2 = dl^2 + 2u_{ik}dx_i dx_k, \tag{2.18}$$

where u_{ik} is the strain tensor, defined as

$$u_{ik} = \frac{1}{2}\big(\frac{\partial u_i}{\partial x_k} + \frac{\partial u_k}{\partial x_i} + \frac{\partial u_l}{\partial x_i}\frac{\partial u_l}{\partial x_k}\big). \tag{2.19}$$

Clearly, along with deformations arise internal forces that try to bring the body back to equilibrium. The forces acting on a small portion of the body can be written as the sum of forces acting on its counterparts, $\int F_i dV$, with F_i being the i_{th} component of the force per unit volume. However, it is clear from Newton's third law that the internal forces should cancel, so any non-zero contribution to this integral must come from forces acting on this body from the outside, i.e. forces acting on its surfaces. Therefore, the integral over the volume can be written as an integral over the surface enclosing the volume if the integrand F_i is the divergence of a second rank tensor, σ_{ik}, which is called the stress tensor:

$$\int F_i dV = \oint \sigma_{ik} df_k = \int \frac{\partial \sigma_{ik}}{\partial x_k} dV. \tag{2.20}$$

2.3.2 Why is Stress a Tensor?

It is clear that strain is a tensor because displacement is a vector of three components, with each component generally being a function of all coordinates. First derivatives with respect to these coordinates results in nine elements that define the strain tensor. However, the fact that stress is also a tensor is not that straightforward.

The stress tensor, more formally known as the Cauchy stress tensor [18], is used to indicate the state of stress at any point in a continuous body, e.g. what are the forces per unit area acting on each point due to the rest of the body.

Why are nine components needed to define this state? Why isn't three enough? The key to understand this is the fact that the stress tensor aims to identify the forces acting on a point inside a body **caused by other parts of the body**. Even though the net force acting on a point has three components, one needs many more to specify which parts of the body are exerting which forces. For a better understanding, consider figure 2.4.

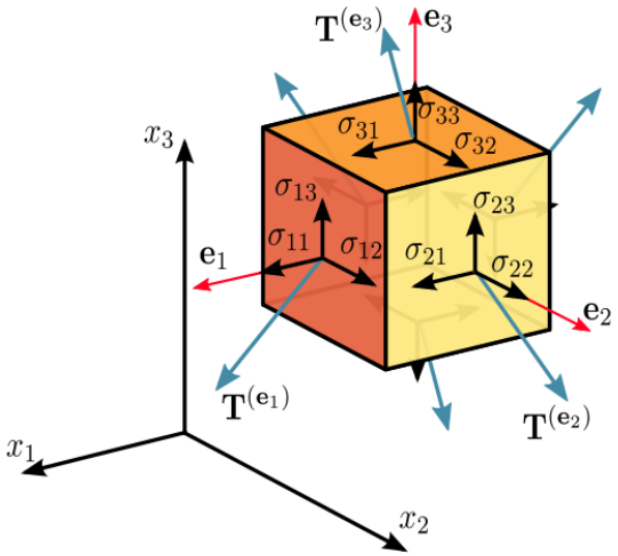

Figure 2.4: Forces T^{e_i} acting on 3 sides of a cube. For each side, one needs 3 components to completely specify the force per unit area, which are labeled as σ_{ij}, where i is the index of the surface and j goes from 1 to 3, indicating the 3 components of the force T^{e_i} acting on surface i.

How many components are needed to indicate the state of stress of a cube of volume V? If there are three forces T^{e_i} acting on three surfaces, then three components are needed for each surface, totaling nine, and justifying the number of elements in the stress tensor. However, this picture is misleading, because there might be more forces acting on the remaining surfaces of the cube. So, in total, one needs to account for six forces acting on six different surfaces, requiring $6 \times 3 = 18$ components. So why doesn't the stress tensor have 18 components? Again, it has to do with the purpose of the stress tensor; it indicates the state of stress at a **point**, not a volume. Therefore, to apply this picture for a point, the limit $V \to 0$ has to be taken, which makes the opposite surfaces of the cube collapse onto one surface. Indeed, one can only define three orthogonal surfaces passing through a point (figure 2.5).

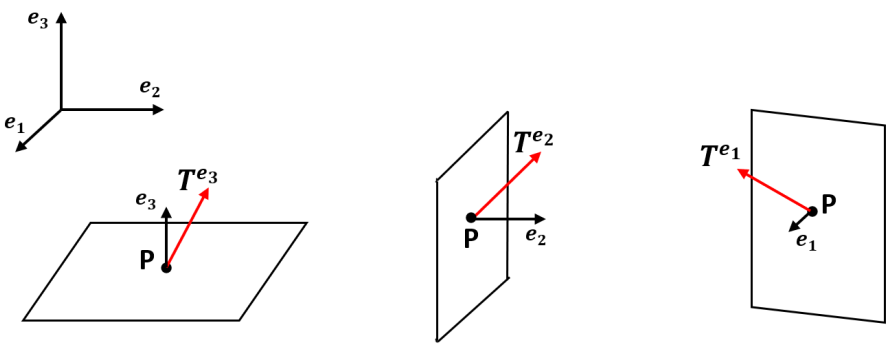

Figure 2.5: Only 3 orthogonal surfaces can be defined passing through point P. These surfaces have directions determined by the unit vectors e^i. On each surface, a force T^{e_i} is exerted.

In this framework, the component σ_{ij} is defined as:

$$\sigma_{ij} = \lim_{dA \to 0} \frac{T_i^{e_j}}{dA}, \tag{2.21}$$

which is the ratio of the i_{th} component of the force acting on surface j to the area of the surface, in the limit of vanishing area. To emphasize, one thinks of three forces acting on a point in the sense that these forces result from different parts of the body. The force T^{e_3} is exerted by the parts of the body just above and below point P, the force T^{e_2} is exerted by the parts of the body just to the right and left of P, etc. This can be related to the definition in equation 2.20 firstly by noting that the i-th component of the net force acting on point P is:

$$T_i = T_i^{e_1} + T_i^{e_2} + T_i^{e_3}, \tag{2.22}$$

which is simply the statement that the net force acting on P is the sum of forces acting from different parts of the body. The force per unit volume F (used in the definition of stress in equation 2.20) can be easily obtained as

$$F_i = \frac{dT_i}{dV} = \frac{\partial T_i^{e_1}}{\partial x_1 dA} + \frac{\partial T_i^{e_2}}{\partial x_2 dA} + \frac{\partial T_i^{e_3}}{\partial x_3 dA}. \tag{2.23}$$

In the limit of vanishing volume, this reduces to:

$$F_i = \sum_j \frac{\partial \sigma_{ij}}{\partial x_j}. \tag{2.24}$$

At mechanical equilibrium, the net force on any point inside the body must be zero:

$$F_i = \sum_j \frac{\partial \sigma_{ij}}{\partial x_j} = 0, \tag{2.25}$$

which can be solved (along with similar equations for the other components of the force) to obtain the stress tensor, if the boundary conditions are specified, which are simply given by the net forces being applied on the surface of the body. If these forces do not result in a net torque on the system, then it can be shown that the stress tensor will be symmetric ($\sigma_{ij} = \sigma_{ji}$).

2.3.3 The Thermodynamics of Deformation

Consider some deformed body, and suppose that the deformation is changed in such a way that the displacement vector is changed by an infinitesimal amount δu_i. The work done by the internal stresses in this change can be expressed as the integral over the volume of force times displacement

$$\int \delta W dV = \int \frac{\partial \sigma_{ik}}{\partial x_k} \delta u_i dV, \tag{2.26}$$

which, after integrating by parts and setting the surface term to 0, leads to the work done (per unit volume)

$$\delta W = -\sigma_{ik} \delta u_{ik}, \tag{2.27}$$

which can be used to find the infinitesimal change in the free energy per unit volume [3]

$$dF = -SdT + \sigma_{ik} du_{ik}. \tag{2.28}$$

This shows that the stress and strain tensors are conjugate thermodynamic variables (like entropy and temperature), related by

$$\sigma_{ik} = \frac{\partial F}{\partial u_{ik}}. \tag{2.29}$$

2.3.4 Hooke's Law

In order to apply these formulae, the free energy as a function of these elastic tensors must be known. For small displacements[4], it can be expanded in a Taylor series up to first non-vanishing terms (the linear term vanishes because $\sigma_{ik} = \frac{\partial F}{\partial u_{ik}} = 0$ for an underformed body)

$$F = \mu(u_{ik} - \frac{1}{3}\delta_{ik} u_{ll})^2 + \frac{1}{2} K u_{ll}^2, \tag{2.30}$$

which is basically Hooke's law in tensorial form. The first term is pure shear, meaning that this term causes the body to change its shape while preserving its

[3] Starting from this equation and onwards, the letter F is used for the free energy, not to be confused with the force in the previous section.

[4] also in this case, the second order terms in equation 2.19 are ignored.

volume and so μ is called the shear modulus. The second term represents compression, meaning that the body preserves its shape, while changing its volume, and so K is called the modulus of compression. With this expression for the free energy, the stress tensor is given by

$$\sigma_{ik} = K u_{ll} \delta_{ik} + 2\mu (u_{ik} - \frac{1}{3} \delta_{ik} u_{ll}). \tag{2.31}$$

Representing the elastic effects of a body through a free energy allows for the incorporation of said effects in the Phase-Field model, which was first done to explain the Grinfeld Instability.

2.4 Grinfeld Instability

2.4.1 Traditional Approach

Elastic effects can strongly influence the morphology of materials and consequently influence material properties and phase transformations. An extensively studied phenomenon that shows such influence is the surface instability of a uniaxially strained solid in contact with its melt, known as Grinfeld instability [19]. A schematic diagram of a typical experimental setup is shown in figure 2.6.

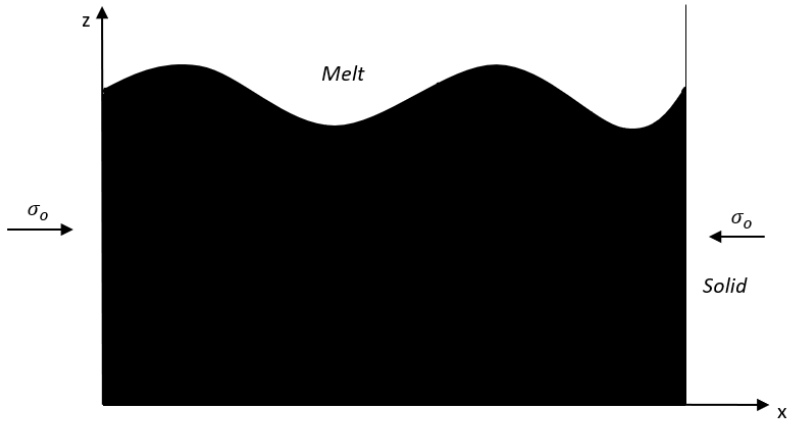

Figure 2.6: A uniaxially stressed solid in contact with its melt. The surface of the solid is corrugated.

Qualitatively speaking, the valleys on the surface will be more stressed than the hills, which can be relieved through diffusion from valleys to hills and phase transformation from solid to liquid. These, in turn, cause the grooves to grow further, increasing the stress gradient and allowing for more diffusion. This feedback loop is the source of the instability. More precisely, there is a difference in

chemical potential between the solid and its melt, given by:

$$\Delta\mu = \frac{1-\nu^2}{2E}(\sigma_{tt} - \sigma_{nn})^2 + \gamma\tilde{\kappa}, \tag{2.32}$$

where σ_o is the external stress, ν is the Poisson ratio, $E = \frac{9\kappa\mu}{\mu+3\kappa}$ is Young's modulus, σ_{tt} and σ_{nn} are the stresses along the tangential and normal directions of the surface, γ is the surface tension, and $\tilde{\kappa}$ is the curvature. This difference drives mass transport by diffusion and condensation/evaporation, the latter being governed by an equation relating the growth of the surface to this chemical potential difference

$$v_n = -\Gamma\Delta\mu, \tag{2.33}$$

where v_n is the growth velocity of the surface (normal to itself) and Γ is a kinetic coefficient. It is possible to rewrite this equation in terms of the profile of the surface $h(x)$

$$\frac{\partial h}{\partial t} = \Gamma\frac{1}{\sqrt{1+h^2}}\left[\gamma\tilde{\kappa} + \frac{1-\nu^2}{2E}(\sigma_{tt} - \sigma_{nn})^2\right]. \tag{2.34}$$

On the other hand, if the transport is surface diffusion, then the equation governing it stems from a continuity equation

$$v_n = -\nabla_s j_s = -\nabla_s(-D\nabla_s\mu) = D\nabla^2\mu. \tag{2.35}$$

Or, in terms of the surface profile

$$\frac{\partial h}{\partial t} = D\frac{1}{\sqrt{1+h^2}}\frac{\partial^2\mu}{\partial s^2}. \tag{2.36}$$

For a given surface profile, it is possible (in essence) to obtain the stress tensor as a function of this profile by imposing mechanical equilibrium:

$$\frac{\partial\sigma_{ij}}{\partial x_j} = 0, \tag{2.37}$$

along with the boundary conditions $\sigma_{ij}n_j$=0 (no mechanical force normal to the surface because the solid and its melt are at equilibrium), and the conditions for uniaxial strain: as $z \to \infty$, $\sigma_{zz} = 0$ and $\sigma_{xx} = \sigma_o$.

If the surface profile is initially $h = h_o sin(qx)$, with a small amplitude, then it is possible to do a linear stability analysis and see the behavior at short times. Such an analysis results in two dynamic equations for the profile obtained from equations 2.34, 2.36, and 2.37

$$\frac{\partial h}{\partial t} = -\Gamma\big[\gamma q^2 - 2\frac{1-\nu^2}{E}\sigma_o^2 q\big]h, \tag{2.38}$$

$$\frac{\partial h}{\partial t} = -\Gamma\big[\gamma q^4 - 2\frac{1-\nu^2}{E}\sigma_o^2 q^3\big]h, \tag{2.39}$$

both of which show the existence of a critical wavenumber $q_c = 2\frac{1-\nu^2}{E}\frac{\sigma_o^2}{\gamma}$ below which the profile is unstable, and above which it is stable. Therefore, there is a range of wavelengths $[0, q_c]$ which are unstable due to the external stress.

This problem contains all the ingredients necessary to model it as a phase-field coupled to an elastic field, which is described below.

2.4.2 Phase Field Modeling

Another way of modeling this instability is through the phase field model [6]. As previously mentioned, the phase field model is a convenient way to simulate free-boundary problems, however it does not inherently contain elastic effects besides surface tension. This issue is resolved by defining an elastic field u_{ij} and coupling it to the phase field through a free energy:

$$F(\phi, u_{ij}) = \int \left[f_t(\phi, u_{ij}) + \frac{l^2}{2}|\nabla\phi|^2 \right], \tag{2.40}$$

where f_t is the bulk free energy density, given by

$$f_t(\phi, u_{ij}) = \frac{1}{a}\phi^2(\phi^2-1)^2 + \frac{\epsilon^2}{2\kappa}g^2(\phi) + \epsilon g(\phi)\vec{\nabla}.\vec{u} + f_{el}(\phi, u_{ij}). \tag{2.41}$$

The first term is the potential well of the phase field, the second term is a shift in the reference energy due to the fact that the strain reference is that of a uniaxially strained solid (with $g(\phi) = \phi^2/2 - \phi^4/4$), the third term is a coupling term, and finally the forth term is the elastic contribution to the free energy:

$$f_{el}(\phi, u_{ij}) = \frac{\kappa}{2}(\vec{\nabla}.\vec{u})^2 + g(\phi)\mu\sum_{ij}(u_{ij} - \frac{\delta_{ij}}{d}\vec{\nabla}.\vec{u})^2. \tag{2.42}$$

By definition, the stress tensor is given by

$$\sigma_{mn} = \frac{\delta F}{\delta u_{mn}}, \tag{2.43}$$

where indices m and n have been used in order to avoid confusion with the dummy indices found in the free energy itself. The terms contributing to this variational derivative are those containing $\vec{\nabla}.\vec{u}$ and the one proportional to μ. First, to vary with respect to u_{mn} it is best to separate these terms in the following manner:

$$\begin{aligned} \epsilon g(\phi)\vec{\nabla}.\vec{u} &= \epsilon g(\phi)\sum_i u_{ii} = \epsilon g(\phi)\sum_{ij} u_{ij}\delta_{ij} \\ &= \epsilon g(\phi)\big[u_{mn}\delta_{mn} + \sum_{i\neq m, j\neq n} u_{ij}\delta_{ij}\big], \end{aligned} \tag{2.44}$$

$$\begin{aligned}\frac{\kappa}{2}(\vec{\nabla}.\vec{u})^2 &= \frac{\kappa}{2}\Big[\sum_i u_{ii}\Big]^2 = \frac{\kappa}{2}\Big[\sum_{ij} u_{ij}\delta_{ij}\Big]^2 \\ &= \frac{\kappa}{2}\big[u_{mn}\delta_{mn} + \sum_{i\neq m, j\neq n} u_{ij}\delta_{ij}\big]^2 \\ &= \frac{\kappa}{2}\big[(u_{mn}\delta_{mn})^2 + (\sum_{i\neq m,j\neq n} u_{ij}\delta_{ij})^2 + 2u_{mn}\delta_{mn}\sum_{i\neq m,j\neq n} u_{ij}\delta_{ij}\big],\end{aligned} \tag{2.45}$$

$$\begin{aligned}g(\phi)\mu\sum_{ij}\big(u_{ij} - \frac{\delta_{ij}}{d}\vec{\nabla}.\vec{u}\big)^2 &= g(\phi)\mu\sum_{ij}\big(u_{ij} - \frac{\delta_{ij}}{d}u_{mn}\delta_{mn} - \frac{\delta_{ij}}{d}\sum_{ij\neq mn} u_{ij}\delta_{ij}\big)^2 \\ &= g(\phi)\mu\big(u_{mn} - \frac{\delta_{mn}}{d}u_{mn}\delta_{mn} - \frac{\delta_{mn}}{d}\sum_{ij\neq mn} u_{ij}\delta_{ij}\big)^2 \\ &\quad + g(\phi)\mu\sum_{ij\neq mn}\big(u_{ij} - \frac{\delta_{ij}}{d}u_{mn}\delta_{mn} - \frac{\delta_{ij}}{d}\sum_{ij\neq mn} u_{ij}\delta_{ij}\big)^2.\end{aligned} \tag{2.46}$$

Now the variation becomes straightforward:

$$\delta\Big(\epsilon g(\phi)\vec{\nabla}.\vec{u}\Big) = \epsilon g(\phi)\delta_{mn}\,\delta u_{mn}\,, \tag{2.47}$$

$$\begin{aligned}\delta[\frac{\kappa}{2}(\vec{\nabla}.\vec{u})^2] &= \frac{\kappa}{2}(2u_{mn}\delta_{mn}u_{mn}\delta_{mn} + 2\delta_{mn}\delta u_{mn}\sum_{i\neq m,j\neq n} u_{ij}\delta_{ij}) \\ &= (\kappa\vec{\nabla}.\vec{u})\delta_{mn}\delta u_{mn},\end{aligned} \tag{2.48}$$

$$\begin{aligned}\delta\Big[g(\phi)\mu\sum_{ij}\big(u_{ij} - \frac{\delta_{ij}}{d}\vec{\nabla}.\vec{u}\big)^2\Big] &= 2g(\phi)\mu\big(u_{mn} - \frac{\delta_{mn}}{d}\sum_{ij} u_{ij}\delta_{ij}\big)(\delta u_{mn} - \frac{\delta_{mn}}{d}\delta u_{mn}\delta_{mn}) \\ &\quad + 2g(\phi)\mu\sum_{ij\neq mn}\big(u_{ij} - \frac{\delta_{ij}}{d}\sum_{ij} u_{ij}\delta_{ij}\big)(-\frac{\delta_{ij}}{d}\delta u_{mn}\delta_{mn}) \\ &= 2g(\phi)\mu\big(u_{mn} - \frac{\delta_{mn}}{d}\vec{\nabla}.\vec{u}\big)\delta u_{mn},\end{aligned} \tag{2.49}$$

which finally results in (after changing the dummy indices mn to ij)

$$\sigma_{ij} = (\epsilon g(\phi) + \kappa\vec{\nabla}.\vec{u})\delta_{ij} + 2\mu g(\phi)\big[u_{ij} - \frac{\delta_{ij}}{d}\vec{\nabla}.\vec{u}\big]. \tag{2.50}$$

The equilibrium equation for the elastic field is:

$$\begin{aligned}\sum_j \frac{\partial\sigma_{ij}}{\partial x_j} &= \epsilon\frac{\partial g(\phi(r))}{\partial x_i} + \kappa\sum_j \frac{\partial}{\partial x_i}\frac{\partial u_j}{\partial x_j} + 2\mu\sum_j \frac{\partial}{\partial x_j}g(\phi)\big[u_{ij} - \frac{\delta_{ij}}{d}\vec{\nabla}.\vec{u}\big] \\ &= 0.\end{aligned} \tag{2.51}$$

This equation is solved perturbatively in μ/κ. The zeroth order term, after multiplying it by $\sum_i \frac{\partial}{\partial x_i}$, gives:

$$\epsilon\nabla^2 g(\phi) + \kappa \sum_{ij} \frac{\partial}{\partial x_i}\frac{\partial}{\partial x_j}\frac{\partial u_j}{\partial x_i} = 0. \tag{2.52}$$

The solution of which is a trick first introduced by Onuki [20]:

$$\frac{\partial u_j}{\partial x_i} = -\frac{\epsilon}{\kappa}\frac{\partial d_j}{\partial x_i}, \tag{2.53}$$

with the vector d defined by:

$$\nabla^2 d_j = \frac{\partial g}{\partial x_j} \; or \; d_j = \nabla^{-2}\frac{\partial g}{\partial x_j}, \tag{2.54}$$

where ∇^{-2} is the inverse Laplacian. This allows for the rewriting of equation 34 as a Poisson equation:

$$\nabla^2 \frac{\partial u_i}{\partial x_j} = -\frac{\epsilon}{\kappa}\nabla_i \nabla_j g. \tag{2.55}$$

The right hand side is symmetric in i and j, and so $u_{ij} = \frac{1}{2}(\frac{\partial u_i}{\partial x_j} + \frac{\partial u_j}{\partial x_i}) = \frac{\partial u_i}{\partial x_j}$.

Expanding the trace of the strain as a function of μ/κ, $\vec{\nabla}.\vec{u} = f_o + \frac{\mu}{\kappa} f_1 ...$[5], and replacing it in equation 2.51 (while again multiplying by $\sum_i \frac{\partial}{\partial x_i}$) gives the equation first order in μ/κ:

$$\nabla^2 f_1 = -2\sum_{ij} \frac{\partial}{\partial x_i}\frac{\partial}{\partial x_j}\left[g(u_{ij} + \frac{\delta_{ij}}{d}\frac{\epsilon}{\kappa}g)\right]. \tag{2.56}$$

Finally the equation for the phase field is given by $\frac{\partial \phi}{\partial t} = -\Gamma\frac{\delta F}{\delta \phi}$, which can be cast into dimensionless form by rescaling $x \to x/\lambda$, where λ is some characteristic length scale, such as the wavelength of the perturbation, $t \to t\Gamma/\lambda^2$, $\beta = \lambda^2/a$, $\epsilon' = l\sqrt{a}/\lambda$, $c = \mu a \epsilon^2/\kappa^2$:

$$\frac{\partial \phi}{\partial t} = -\beta\big[(1-\phi)(2\phi - 4\phi^2) - \epsilon'^2\nabla^2\phi + cg'(\phi)h(\phi)\big], \tag{2.57}$$

with

$$h(\phi) = [f_1 + \sum_{ij}(u_{ij} + \frac{\delta_{ij}}{d}g)^2]. \tag{2.58}$$

Numerically, equation 2.55 is solved first by the relaxation method, the solution is then used to solve equation 2.56 again by the relaxation method, and finally both solutions are used to solve equation 2.57 using Euler's Method. Throughout, due

[5] $f_0 = u_{xx} + u_{yy}$ is easily obtained from equation 2.55 as $-\frac{\epsilon}{\kappa}g$.

to the rapidly varying functions involved, the isotropic Laplacian was used [2]. Numerical details can be found in appendix A.

As it stands, this model is not appropriate for modeling biological creatures, due to the two main reasons mentioned in the introduction: 1) Biological creatures should be modeled by a conservative phase-field (at least within the time frame of interest), and 2) The instability should not grow indefinitely; it should be limited. The motivation behind these adjustments is obtained from a peculiar little creature known as Trichoplax adhaerens.

2.5 Trichoplax Adhaerens

Trichoplax Adhaerens is a flat multi cellular creature in the phylum Placozoa, which lacks any organs or internal structure. Lacking sensory and muscle cells, it moves using cilia on its external surface, which are leg-like organelles that more or less fire randomly and independently, with the occasional coordinated motion in the presence of food [12]. This results in some peculiar morphological dynamics, buckling being of particular interest; when close sections of the creature move towards each other, one can observe buckling on the surface, akin to pinching one's skin. We propose that this is due to a build up of stress in the creature that is released in the form of an instability similar to Grinfeld's instability (see figure 2.7).

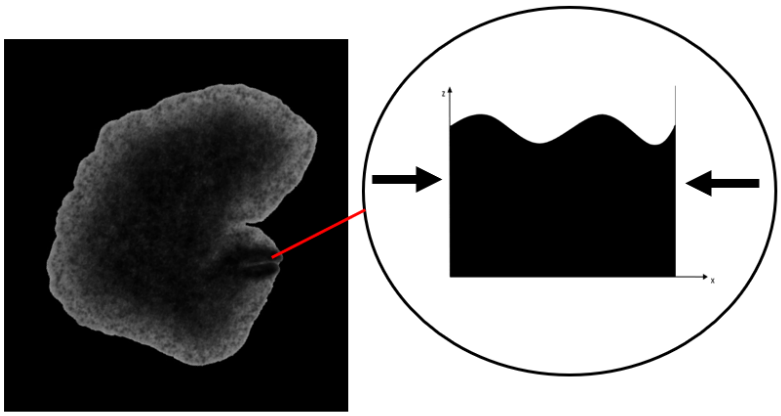

Figure 2.7: The buckling at the surface can be explained by the fact that opposite moving parts of the creature impose a stress between them that results in an instability resembling Grinfeld's Instability.

Therefore, it is possible to model this instability using a phase-field coupled to an elastic field, where the phase-field's two minima have the meaning of "cell" ($\phi = 1$) and "outside of cell" ($\phi = 0$). Of course, with such an understanding, no

phase transformation can occur, which implies that the dynamics is conservative:

$$\frac{\partial \phi}{\partial t} = \beta \nabla^2 \big(\frac{\delta F}{\delta \phi} \big), \tag{2.59}$$

where F is the free energy used for Grinfeld's instability, so:

$$\frac{\delta F}{\delta \phi} = (1-\phi)(2\phi - 4\phi^2) - \epsilon'^2 \nabla^2 \phi + c g'(\phi) h(\phi). \tag{2.60}$$

To limit the growth of the instability, we consider the parameter c, which is related to the external forcing, to be dependent on time, $c = c(t)$. Actually, it should be decreasing with time, i.e. the external stress should be decreasing. This will limit the growth in different ways, depending on the actual form of the function. We study linear and power-law decay.

Chapter 3

Methods and Results

3.1 Grinfeld Instability Results

As a check for our algorithm, we reproduce results found in [6]. We apply equation 2.57 for a system with parameters $\delta x = 0.01$, $\delta t = 0.05$, $\beta = 1$, $\epsilon = 0.01$, $Lx = Ly = 256$ (in units of δx), and $c = 6.2$. First we set up a corrugation at position $y = 0.73Ly$, of the form $h(x) = (0.02Ly)\cos(qx)$, with $q = 3\frac{2\pi}{\delta x Ly}$. The boundary conditions are periodic in the horizontal direction and no-flux in the vertical direction. We observe a growing instability, shown in the figures below

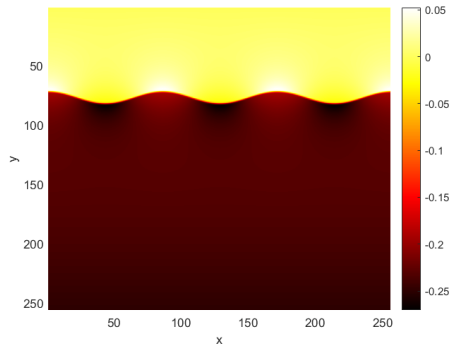

(a) The only non-zero component of the strain tensor, u_{yy}. In the bulk of the solid (lowest point along the y-direction), it is equal to $-g(\phi) = -0.25$, meaning the solid is uniaxially strained along the y-direction.

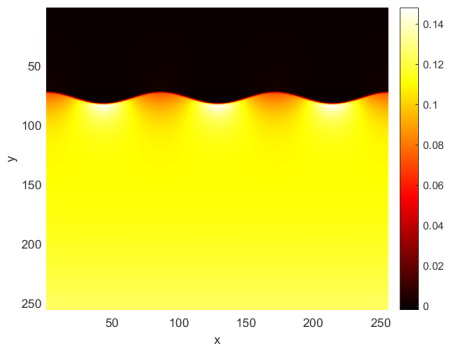

(b) The only non-zero component of the stress tensor, σ_{xx}. In the bulk of the solid (lowest point along the y-direction), it is equal to $g(\phi)/2 = 0.125$. It is also clear that valleys in the profile are more stressed than hills.

Figure 3.1: The stress and strain fields with parameters $Lx = Ly = 256$, $c = 6.2$, and $\epsilon = 0.01$ for the initial profile $h(x) = (0.02Ly)\cos(qx)$.

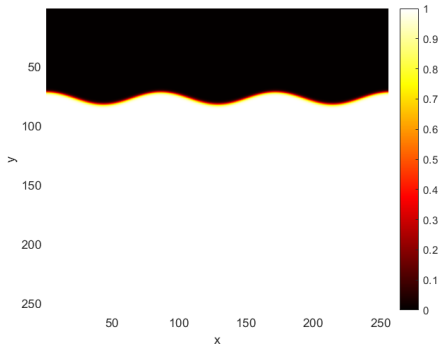

(a) The phase field at $t = 0$, which shows the initial surface profile $h(x) = (0.02Ly)\cos(qx)$.

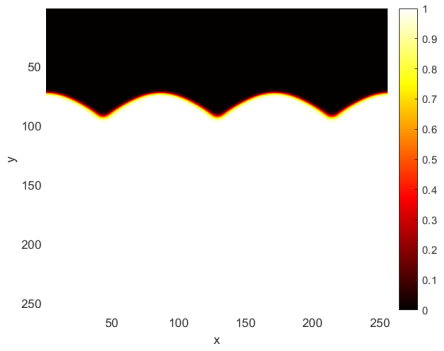

(b) The phase field at $t = 20$. The amplitude of the profile grows and grooves begin to form.

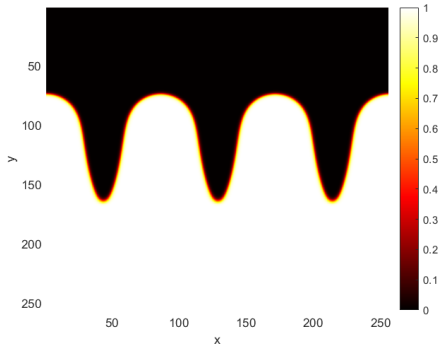

(c) The phase field at $t = 70$. The grooves have gotten deeper due to the instability.

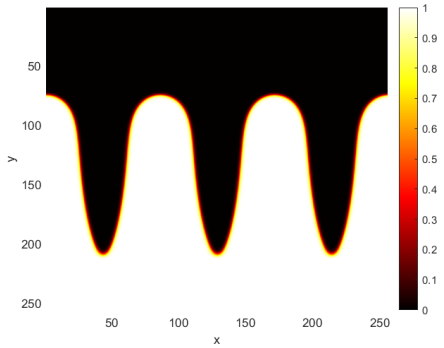

(d) The phase field at $t = 100$. The simulation stops before the grooves reach the boundary.

Figure 3.2: The evolution of the phase field with parameters $Lx = Ly = 256$, $c = 6.2$, and $\epsilon = 0.01$.

For a more quantitative check, it is possible to do a numerical linear stability analysis for different Fourier modes and see how they evolve for small times. In [6] it was found that modes grow independently and exponentially, obeying $exp(w(q)t)$, with $w(q)$ given by the dispersion relation

$$w(q) = Aq - Bq^2 \tag{3.1}$$

with $A \approx 28.2$ and $B \approx 1$. We found a very similar result, with $A \approx 42$ and $B \approx 1.4$, shown in figure 3.3

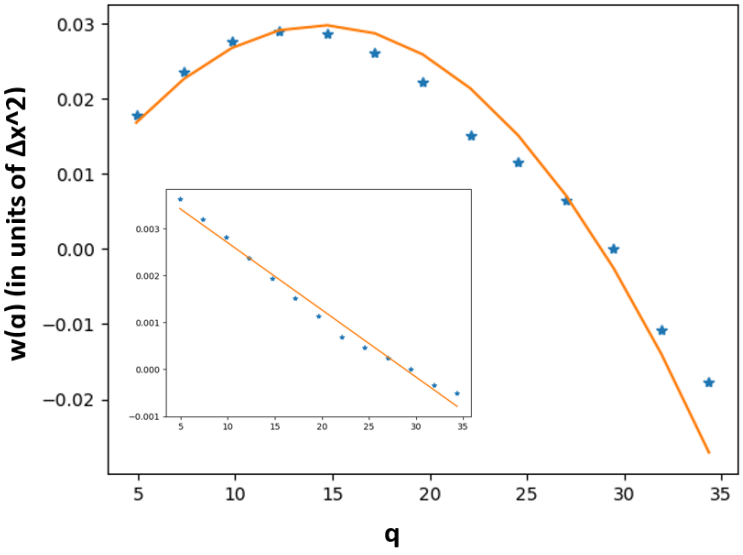

Figure 3.3: Dispersion relation obtained numerically for short times. The inset shows w/q vs q. The system has parameters $Lx = Ly = 256$, $c = 6.2$, and $\epsilon = 0.01$.

There is some discrepancy which can be attributed to the fact that different modes quickly start interacting with each other, making a numerical stability analysis quite difficult. To accurately obtain the dependence of the amplitudes as a function of time, one needs to fine-tune different parameters and see for how long modes grow independently, in order to get a proper exponential dependence, and from it obtain the dispersion relation.

3.2 Extracting Data From Video

The motivation behind the suggested model is mainly due to a video of Placozoa captured in its center of mass frame of reference. With no food source nearby, the creature just moves randomly in all directions, stretching and contracting in many different ways. Sometimes, due to this random motion, it is observed that small parts buckle out of plane, as if to relieve stress. Some snapshots from the video are shown in figure 3.4.

From these snapshots, it is possible to obtain an actual phase field using any image processing tool. The phase field is defined as $\phi = 1$ if the intensity of a pixel is greater than zero, and $\phi = 0$ if the intensity is zero (an example is shown in figure 3.6). This phase field can be used to obtain the position of the center of mass of the creature at all times, along with the area A defined as the total sum

of the field:

$$A = \sum_i \sum_j \phi(i,j), \tag{3.2}$$

$$Xcm = \frac{\sum_i i\phi(i,j)}{A}, \tag{3.3}$$

$$Ycm = \frac{\sum_j j\phi(i,j)}{A}. \tag{3.4}$$

These can be plotted as a function of time to get some idea of the motion of the creature along with the magnitude of its fluctuations. These plots are shown in figure 3.5.

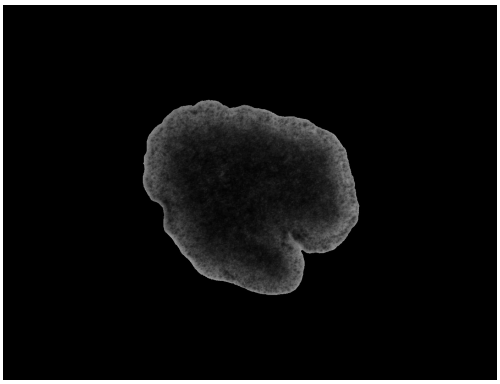

(a) A snapshot from the video (frame 1840).

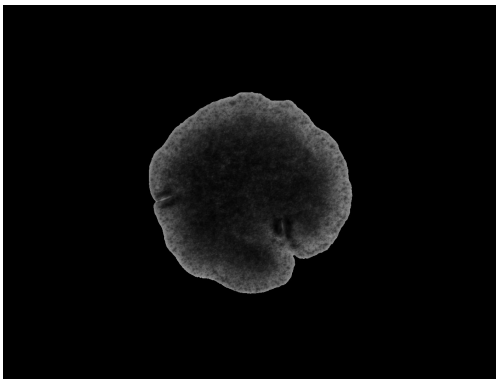

(b) A snapshot from the video (frame 1895). The creature looks more circular. Also, two instances of out-of-plane behavior are observed.

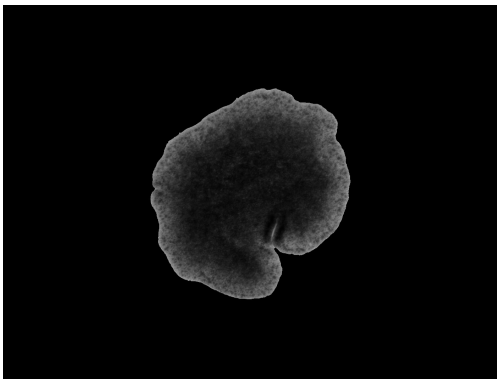

(c) A snapshot from the video (frame 1915). The small buckled part on the left side has relaxed, whereas the other one is still out-of-plane.

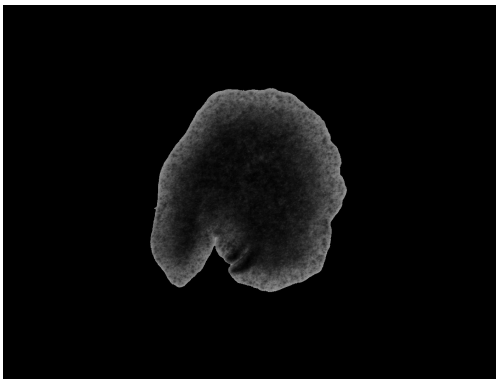

(d) A snapshot from the video (frame 1960). More random motion. The remaining out-of-plane buckling is still sustained.

Figure 3.4: Some snapshots from the video of the creature. They show random motion in all directions and out of plane buckling.

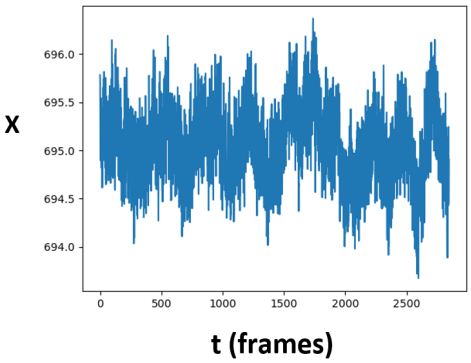

(a) The position of the center of mass along the horizontal direction as a function of time. As expected, it barely moves at all because the video was captured in the center of mass frame.

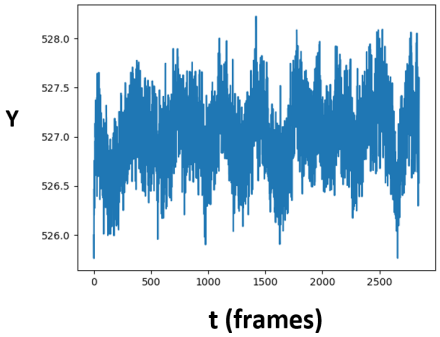

(b) The position of the center of mass along the vertical direction as a function of time. As expected, it barely moves at all because the video was captured in the center of mass frame.

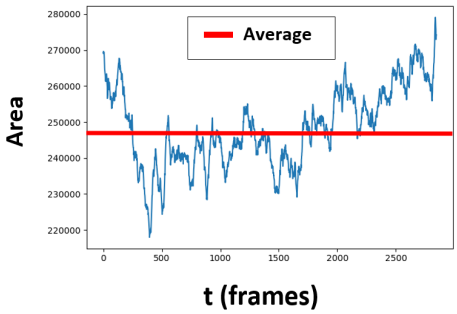

(c) The area of the creature as a function of time. It fluctuates about 5-10% around the average due to random motion, most of which is in-plane stretching and deformation, but some of which is caused by out-of-plane buckling.

Figure 3.5: The position of the center of mass as a function of time (a and b), along with the area as a function of time (c).

As expected, the center of mass barely moves at all due to the fact that the videos were captured in the center of mass frame. Also, the area of the creature fluctuates about 5-10% around the mean value, because of random motion, most of which is in-plane stretching and deformation, but some of which is caused by out-of-plane buckling.

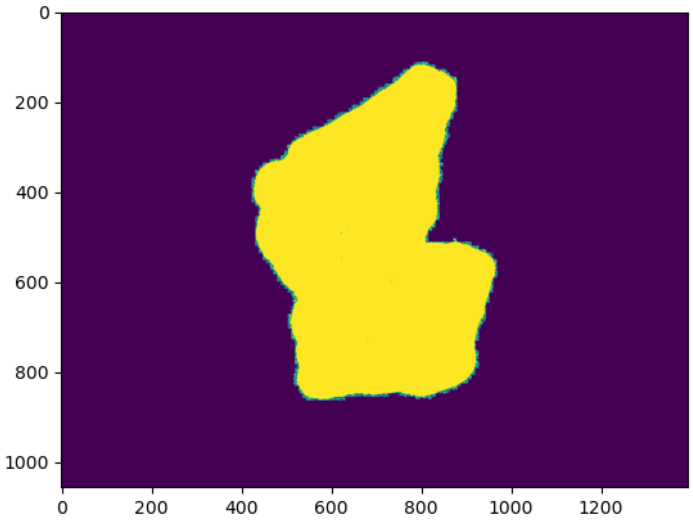

Figure 3.6: A phase field obtained from one frame. Yellow is $\phi = 1$, which corresponds to pixels in the frame that have a non-zero intensity. Dark blue is $\phi = 0$, which corresponds to pixels that have zero intensity.

3.3 Conserved Field With Time-Varying External Forcing

We now move to the analysis of a conserved phase-field with a time-varying external stress. The conserved dynamics is governed by the equation:

$$\frac{\partial \phi}{\partial t} = \nabla^2[(1-\phi)(2\phi - 4\phi^2) - \epsilon'^2\nabla^2\phi + cg'(\phi)h(\phi)], \tag{3.5}$$

and the time-varying external forcing is applied through the parameter $c = c(t)$. Two types of functions are studied: linearly decreasing and power-law decay.

3.3.1 Linear Time Dependence

First the external forcing is decreased linearly as a function of time, starting with an initial value $c_0 = 8$ and $\alpha = 0.1, 0.2$:

$$c(t) = -\alpha t + c_0. \tag{3.6}$$

If c reaches zero, it stays zero for the rest of the simulation. The evolution of the phase field for $\alpha = 0.1$ is shown in figure 3.7.

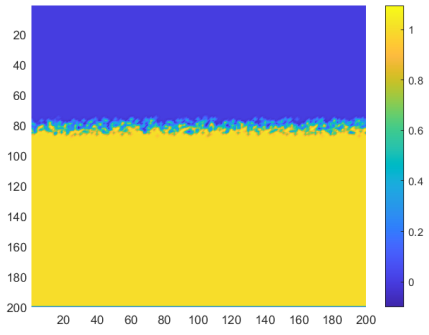

(a) The phase field at $t = 0$, which shows a random initial configuration produced by random seeds near the interface.

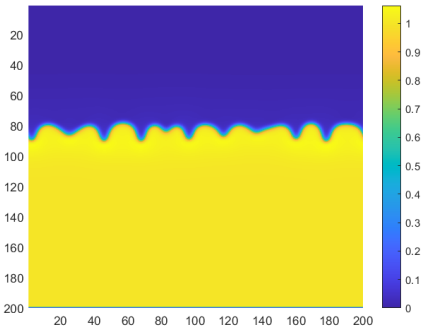

(b) The phase field at $t = 10$. A rough interface is formed.

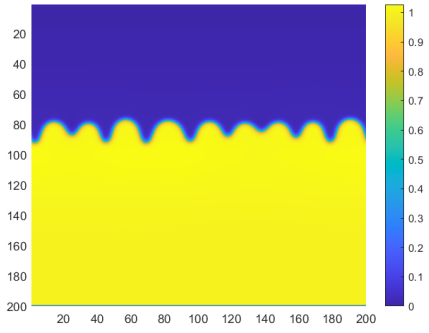

(c) The phase field at $t = 50$. The interface has grown slightly, and at this point $c = 3$.

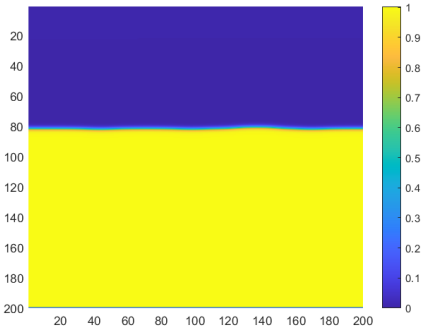

(d) The phase field at $t = 200$. The interface flattens out. c reached zero at $t = 80$.

Figure 3.7: Evolution of the phase field with parameters $Lx = Ly = 200$, $c = -0.1t + 8$, and $\epsilon = \Delta x = 0.3$.

Quantitatively, the evolution of the interface can be tracked by obtaining the structure factor $S(q, t)$ at each time step, which is defined as the Fourier transform of the height-height correlation function:

$$H(x') = \langle [h(x + x') - h(x)]^2 \rangle_x. \tag{3.7}$$

Details of how the structure factor is obtained is given in appendix B. The time evolution of the structure factor is shown in figure 3.8. The initial random seeds quickly form a rough interface with a dominant wavenumber $q \approx 0.9$. It grows fast and reaches a peak at about $t \approx 50$, after which it starts decaying and flattens out at about $t \approx 100$.

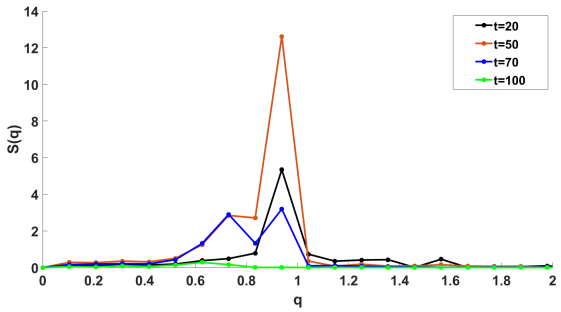

Figure 3.8: The evolution of the structure factor for an initial random surface and $c = -0.1t + 8$.

For a better understanding, we analyze individual Fourier modes by starting with the interface $h = h_0 sin(qx)$ and tracking the amplitude of that mode as a function of time. The results are shown in figure 3.9 for several modes, with wavenumbers $q_n = n\frac{2\pi}{\Delta x L x} = n(0.1047)$, up to $n = 7$.

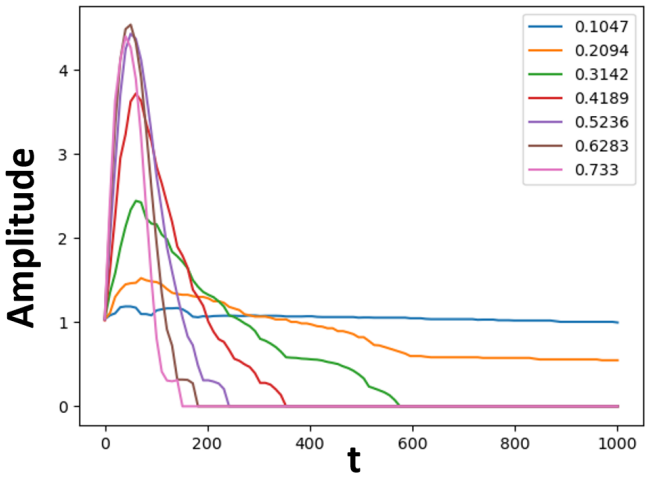

Figure 3.9: Tracking the amplitudes of different Fourier modes for $c = -0.1t + 8$. The first 2 modes, blue and orange, barely grow and take a very long time to decay. This explains why the surface takes a very long time to flatten out completely. Higher modes grow rapidly and reach a peak at roughly the same time $t_{peak} \approx 50$.

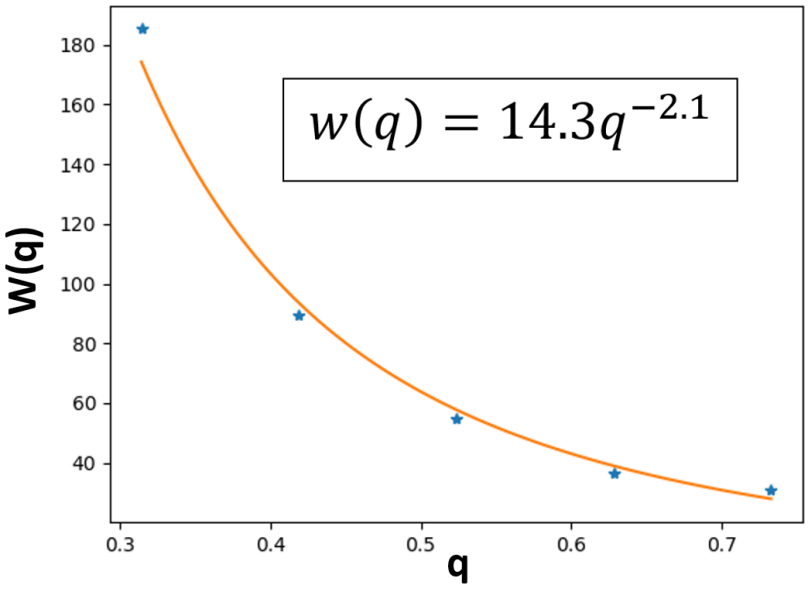

Figure 3.10: The width, defined as root mean squared deviation from the peak position, for different wavenumbers. It defines a natural timescale for the system. $\alpha = -0.1$.

The first two modes barely grow and take a very long time to decay, whereas higher modes grow rapidly and reach a peak at roughly the same time of $t_{peak} \approx 50$. The mode that we start off with stays the dominant mode throughout the simulation (it always has a much larger amplitude than the rest), which means that the profile is not coarsening. It is also interesting to note that the width of the curves, defined as root mean squared deviation from the position of the peak, depends on q as $w(q) \approx 14.3q^{-2.1\pm0.2}$. This is shown in figure 3.10. The widths for the first two wavenumbers could not be extracted because of the length of time required to reach a flat surface. Indeed, one can get sense of this time scale by using the fit for $w(q)$. For example, this gives $w(0.2) = 462$, which means that one has to reach $t \approx 2000$ (about $4w$) in order to flatten out the profile starting with wavenumber $q = 0.2$.

It is clear from the above discussion that the width of each curve defines a natural time scale for the system starting out with a given wavenumber. The same analysis but for $\alpha = -0.2$ leads to $w(q) \approx 9.46q^{-2.3\pm0.1}$, which means that for a larger (negative) slope, the time scales are shorter. Indeed, for $\alpha = -0.2$, c decreases more rapidly and reaches zero at $t = 40$. Also, for this slope, $t_{peak} \approx 20$.

3.3.2 Power-Law Dependence

A more interesting time-dependence for the parameter c is a power law:

$$c(t) = c_0(t+1)^{-\alpha}, \tag{3.8}$$

where c_0 is the initial value of c, and α is the characteristic exponent of decay. The motivation behind this approach is to find a functional dependence on time such that an initial random profile will grow up to a certain amplitude and then stop growing, resembling a "steady state", at least within a small (but not too small) time interval. A linearly decreasing parameter did not achieve this, because the growth and decay happened quickly. The first trial was done for $c_0 = 8$ and $\alpha = 0.25$, which leads quickly to a near-flat interface (figure 3.11).

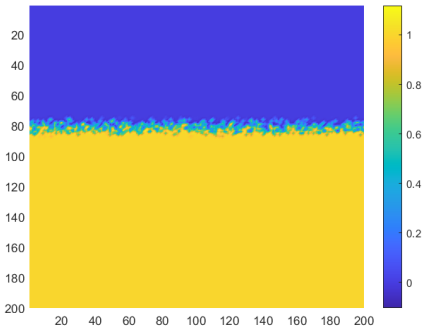

(a) The phase field at $t = 0$, which shows a random initial configuration produced by random seeds between the two phases.

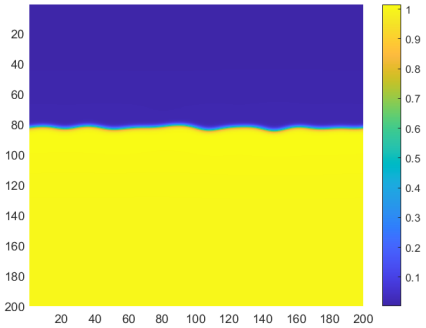

(b) The phase field at $t = 50$. A rough interface is formed.

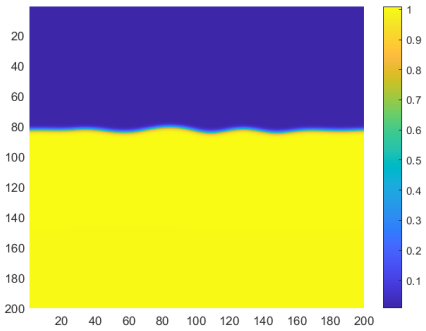

(c) The phase field at $t = 200$. The interface has neither flattened nor grown. However, the amplitude is very small, and complete flattening takes a lot of time due to conservative dynamics.

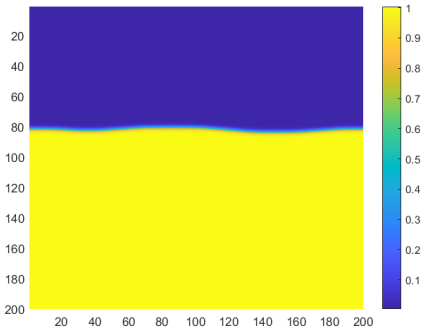

(d) The phase field at $t = 6000$. The interface is still not completely flat, but is less rough than at $t = 50$. The dominant wavenumber has decreased.

Figure 3.11: Evolution of the phase field with parameters $Lx = Ly = 200$, $c = 8(t+1)^{-0.25}$, and $\epsilon = \Delta x = 0.3$.

Quantitatively, the evolution can be tracked by again following the structure factor S(q) shown in figure 3.12.

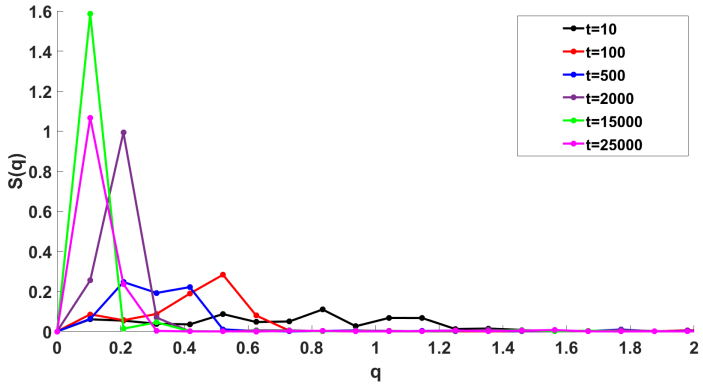

Figure 3.12: The evolution of an initial random configuration with $c(t) = 8(t+1)^{-0.25}$ as seen through the structure factor.

Initially, at $t = 10$, there are many wavenumbers with low amplitudes (black). With time, the surface coarsens, and less wavenumbers contribute with larger amplitudes. Eventually, starting $t \approx 15000$, the dominant wavenumber is the lowest one, and it has a relatively large amplitude (green). At even larger times, the first wavenumber remains the dominant one, however its amplitude decreases very slowly (magenta). It is clear that, if ran long enough, the profile will become flat.

Again, for a better understanding, we analyze individual Fourier modes by starting with the interface $h = h_0 sin(qx)$ and tracking the amplitude of that mode as a function of time. The results are shown in figure 3.13 for several modes, with wavenumbers $q_n = n(0.1047)$, up to $n = 7$. The first mode (blue) grows very slowly. The second mode (orange) grows much faster and reaches a peak before decaying. The simulation is not long enough for it to flatten out. The rest of the modes grow fast, reach a peak, and decay slower than the speed with which they grew, eventually turning flat. It should be noted that the peaks for different modes have different heights, and are reached at different times. Also, the fact that the first mode grows very slowly explains why it is the only one surviving in the structure factor at long times in figure 3.12 (by the time it reaches its peak, all the other modes have decayed to zero). Lastly, it looks as if the shapes of the curves for different wavenumbers look similar, suggesting a universal function on which they should collapse after rescaling. Indeed, rescaling the time axis by $\frac{t-t_p}{w}$, where t_p is the position of the peak and w is the root mean squared deviation from that position, along with rescaling the vertical axis by $\frac{y}{y_p}$ results in a descent, although not perfect, collapse, shown in figure 3.14.

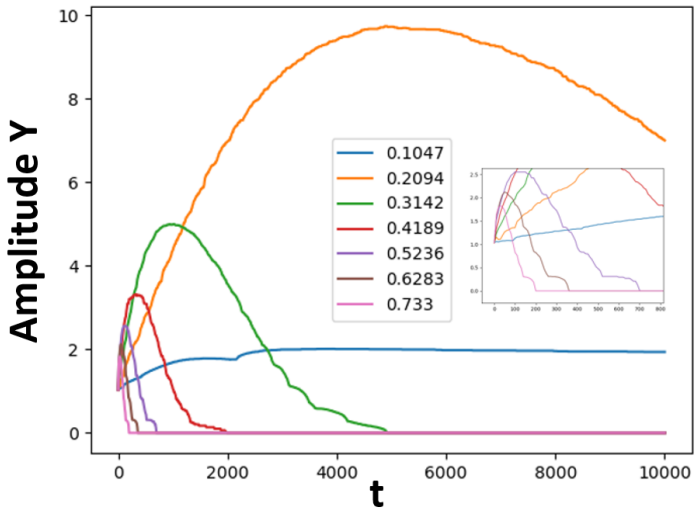

Figure 3.13: Tracking the amplitudes of different Fourier modes for $c = 8(t+1)^{-0.25}$. The first mode (blue) grows very slowly. The second mode (orange) grows much faster and reaches a peak before decaying. The rest of the modes grow fast, reach a peak, and decay slower than the speed with which they grew, eventually turning flat.

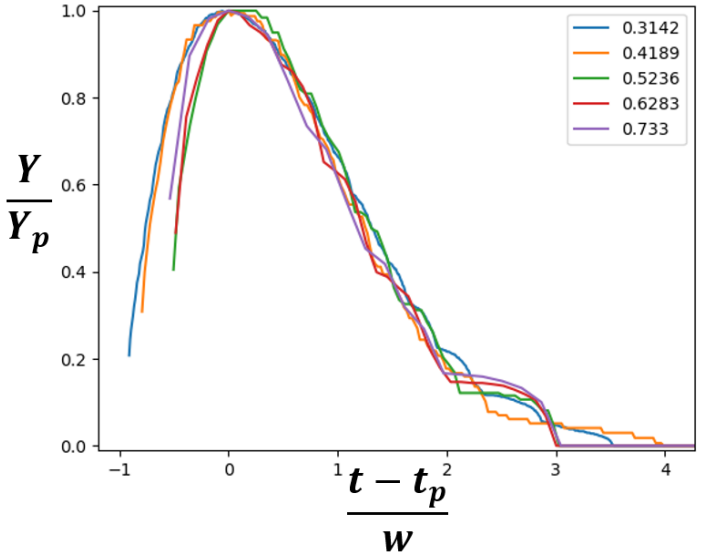

Figure 3.14: Scaled graph of different Fourier modes. The decay-part collapses near perfectly on a Gaussian centered around zero with standard deviation $\sigma = 1.155$.

Next, we study the effect of changing c_0 for the given exponent $\alpha = 0.25$. Needless to say, the behavior of the profile is roughly the same, but with even

less growth because of a smaller c. The best way to see the quantitative difference is to also track the Fourier modes, and plot the peak height y_p, peak position t_p, and curve width w as a function of q for $c_0 = 6, 8$. The results are shown in figure 3.15.

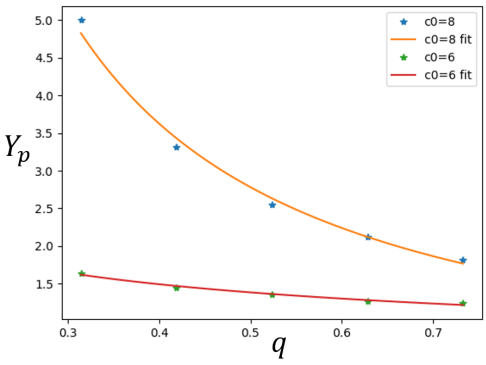

(a) Peak heights as a function of wavenumber for $c_0 = 8$ (orange) and $c_0 = 6$ (red). The fits are power-laws of the form $y_p = 1.22q^{-1.21\pm0.01}$ for $c0 = 8$ and $y_p = 1.1q^{-0.34\pm0.01}$ for $c_0 = 6$.

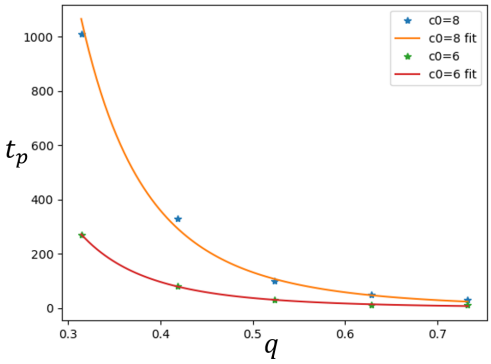

(b) Peak positions as a function of wavenumber for $c_0 = 8$ (orange) and $c_0 = 6$ (red). The fits are power-laws of the form $t_p = 0.6q^{-4.5\pm0.2}$ for $c0 = 8$ and $y_p = 0.135q^{-4.40\pm0.02}$ for $c_0 = 6$.

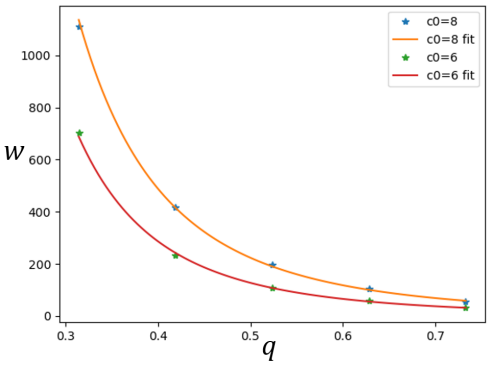

(c) Widths as a function of wavenumber for $c_0 = 8$ (orange) and $c_0 = 6$ (red). The fits are power-laws of the form $y_p = 2q^{-3.50\pm0.03}$ for $c0 = 8$ and $y_p = 1q^{-3.60\pm0.01}$ for $c_0 = 6$.

Figure 3.15: Comparing peak position, peak height, and width of curve for $c_0 = 6, 8$ as a function of wavenumber.

The net result is that reducing c_0 to 6 results in qualitatively similar behavior, but with smaller time and length scales. It is interesting to note that y_p, t_p, and w all exhibit power-law dependence on wavenumber, and the exponents for the widths and peak positions are roughly the same for the different c_0's.

Now, we study $c_0 = 8$ and $\alpha = 0.15$. It is expected that an initial random

profile will grow much more than the previous cases. Indeed, the evolution is shown in figure 3.16. The growth of the profile is much faster than desired, and the reason for this becomes clear when different Fourier modes are analyzed. It is observed that, for $q = 6q_1$ and $q = 7q_1$, the initial wavenumber does not remain the dominant one; the profile coarsens well before the growth stops (figure 3.17). This means that for an initial random profile, large wavenumbers will, in a sense, boost the growth of smaller ones due to fast coarsening, which will lead to a speedy growth of smaller wavenumbers, and eventually the smallest wavenumber $q = q_1$ will dominate, as seen in figure 3.16*d*.

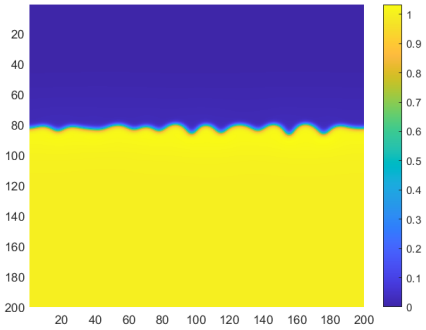

(a) The phase field at $t = 10$. A rough interface has formed composed of many wavenumbers.

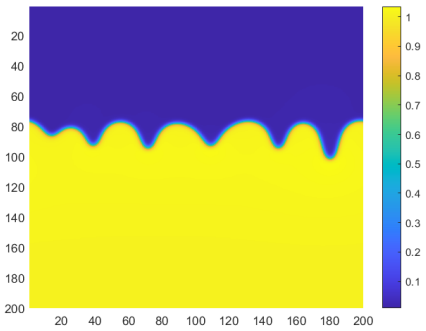

(b) The phase field at $t = 200$. Grooves begin to form.

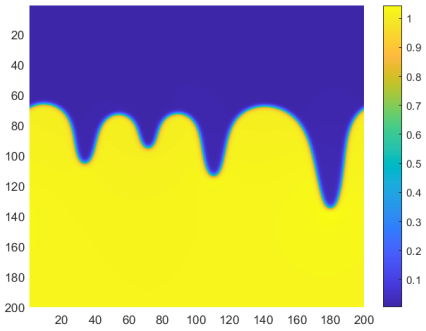

(c) The phase field at $t = 700$. The interface starts to coarsen as grooves become deeper.

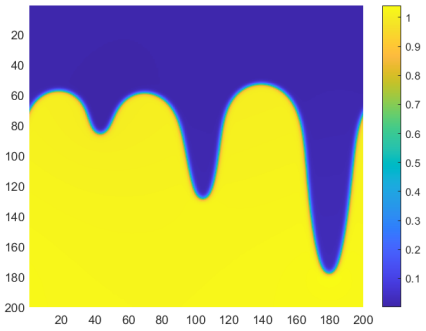

(d) The phase field at $t = 2000$. A dominant groove has appeared which reaches the boundary of the system.

Figure 3.16: Evolution of the phase field with parameters $Lx = Ly = 200$, $c = 8(t + 1)^{-0.15}$, and $\epsilon = \Delta x = 0.3$.

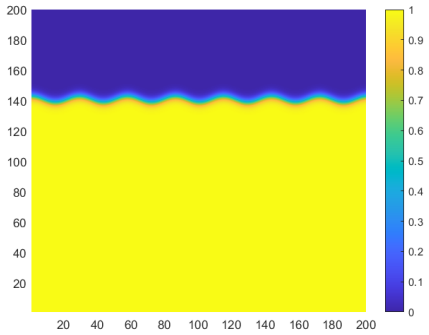

(a) The phase field at $t = 0$. The profile is $h = 0.01cos(q_7 x)$.

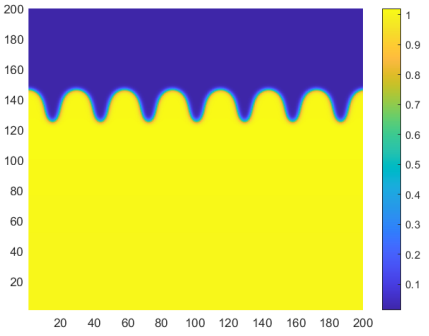

(b) The phase field at $t = 200$. The initial profile has grown and grooves have formed.

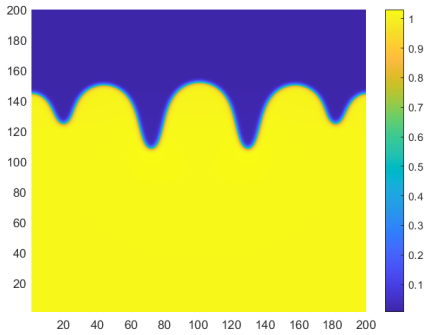

(c) The phase field at $t = 1000$. Different grooves combine together to form larger grooves and an overall profile of a smaller dominant wavenumber. This is coarsening.

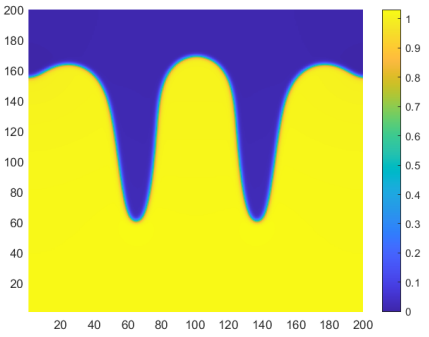

(d) The phase field at $t = 3000$. The new dominant Fourier mode keeps growing while the remaining ones shrink.

Figure 3.17: Evolution of the phase field with parameters $Lx = Ly = 200$, $c = 8(t+1)^{-0.15}$, $\epsilon = \Delta x = 0.3$, and initial profile $h = 0.01cos(q_7 x)$. Coarsening is observed; the initial wavenumber of the profile does not stay the dominant one at longer times.

So far, an analysis of exponents $\alpha = 0.15, 0.25$ have shown that one is too large, and the other too small. Therefore, it is natural now to study $\alpha = 0.2$, with $c_0 = 8$. This also fails to provide a "steady state", but it is much better than $\alpha = 0.15$. The evolution of an initial random profile is shown in figure 3.18.

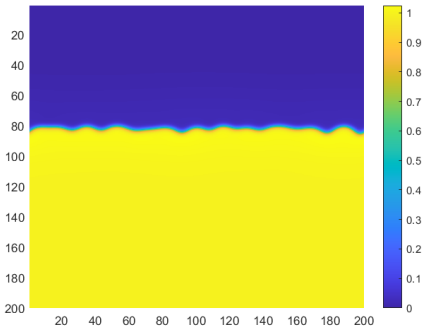

(a) The phase field at $t = 10$. A rough interface has formed.

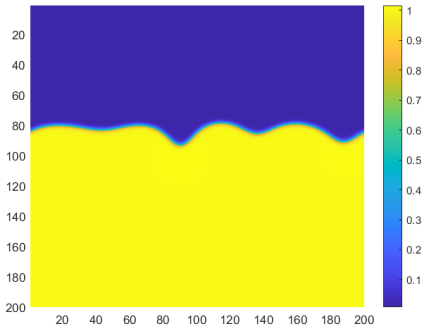

(b) The phase field at $t = 500$. The initial profile has grown and grooves have formed.

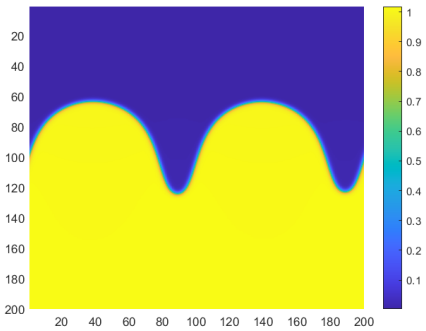

(c) The phase field at $t = 1500$. The profile has coarsened. The dominant wavenumber is clearly q_2.

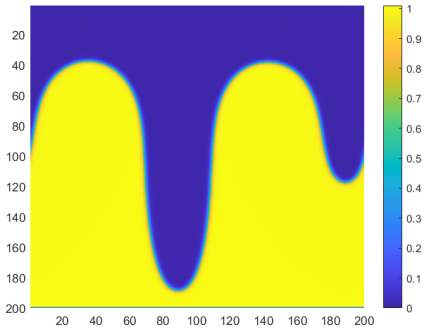

(d) The phase field at $t = 10000$. The profile is still coarsening, but very slowly. The dominant wavenumber is q_1. By this time, the deepest groove has reached the boundary of the box.

Figure 3.18: Evolution of the phase field with parameters $Lx = Ly = 200$, $c = 8(t+1)^{-0.2}$, $\epsilon = \Delta x = 0.3$, and initial random profile. Coarsening is observed, but it is slow.

It is clear that the evolution is closer to the desired "steady-state" regime, but the initial large value of c has caused the deepest groove to reach the boundary of the simulation before the onset of this regime. Therefore, all that is required is a qualitatively similar behavior, but with a shorter time scale and smaller length scale. As discussed above, this can be achieved by changing c_0 to a smaller value. Indeed, the evolution of the phase field for $c(t) = 6(t+1)^{-0.2}$ is shown in in figure 3.19.

Again, for a more quantitative analysis, it is possible to follow the structure factor, shown in figure 3.20. The initial random configuration coarsens until the first wavenumber is left as the dominant one at $t \approx 2000$. Afterwards, the

evolution is just a slow growth, resembling a "steady state" within a small time interval.

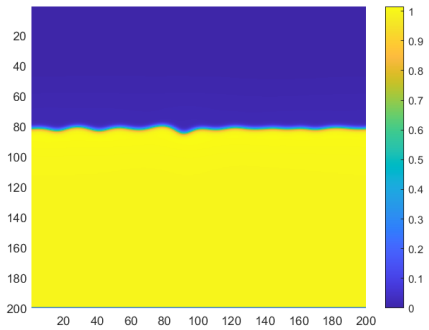

(a) The phase field at $t = 10$. A rough interface has formed.

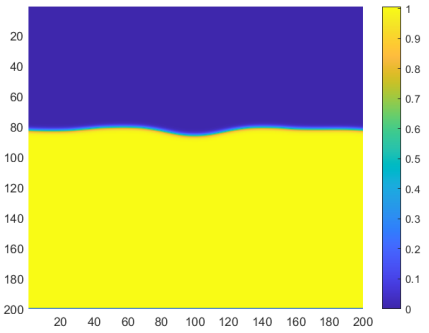

(b) The phase field at $t = 2000$. The profile has coarsened, with a slight increase in amplitude.

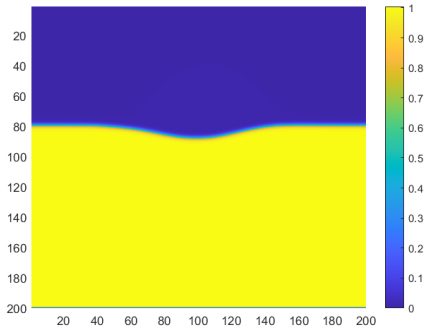

(c) The phase field at $t = 10000$. After more coarsening, the dominant wavelength is $q = q1$, and it is growing slowly.

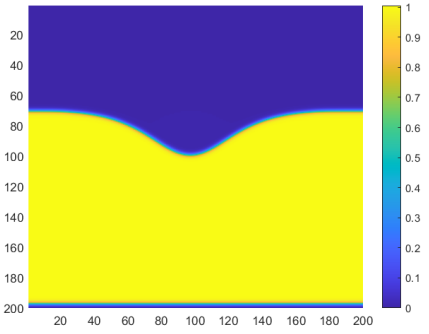

(d) The phase field at $t = 20000$. The amplitude is still increasing, but very slowly.

Figure 3.19: Evolution of the phase field with parameters $Lx = Ly = 200$, $c = 6(t+1)^{-0.2}$, $\epsilon = \Delta x = 0.3$, and initial random profile. The desired "steady state" is achieved; an initial random profile coarsens and eventually leads to a very slow growing profile with dominant wavenumber $q = q_1$

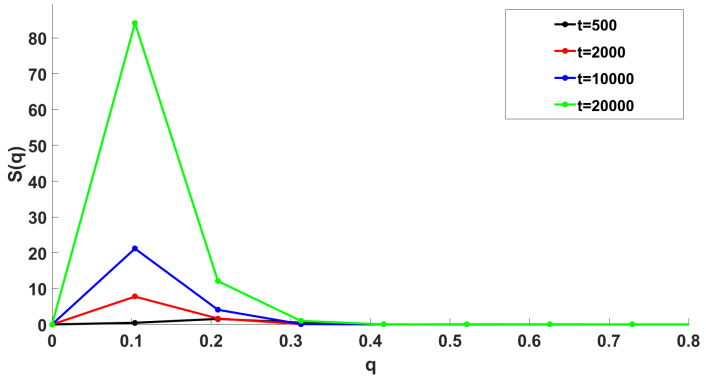

Figure 3.20: The evolution of an initial random configuration with $c(t) = 6(t+1)^{-0.25}$ as seen through the structure factor. The profile coarsens until the first wavenumber is left as the dominant one, which grows very slowly.

3.4 3D simulations

Another advantage of the phase field model is that the equations can be easily generalized to 3 dimensions. However, the simulations can take a very long time, because the speed is of the order N^3, N being the size of the box. In addition to this, the strain tensor now becomes a 3x3 tensor, with 6 unique elements (due to symmetry), which means that 3 additional Poisson equations (eq. 2.55) need to be solved. To start with, we first ran a simulation of a box size $L = 100$ with a random surface at the height $z = 60$ and under constant uniaxial strain ($c = 8$). The results are shown in figure 3.21. To properly see the interface, the isosurface $\phi = 1/2$ is plotted. The initial random seeds form an interface which grows and grooves begin to form. The system is symmetric in x and y because for uniaxial strain, $\sigma_{xx} = \sigma_{yy} \neq 0$. This simple and short simulation took about 24 hours on a high-performance computer.

Alternatively, it is possible to impose a uniaxial stress along one direction, say y, while having no stresses in the other directions. This should break the symmetry between x and y. Indeed, the results are shown in figure 3.22. Since the stress is only along one direction, grooves form along that direction, but not along the other one. This causes stripes to form. This can also be understood by treating each cross section as a 2D system under uniaxial strain with a different initial condition. After they evolve and coarsen, different cross sections will have almost the same Fourier modes active, but with different phases.

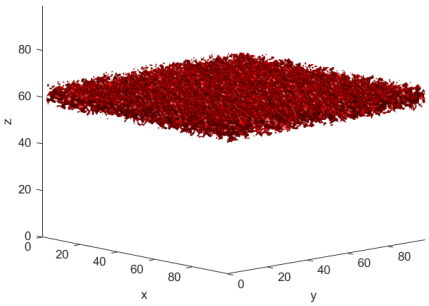

(a) The isosurface $\phi = 1/2$ at $t = 0$, showing a random initial surface at $z = 60$.

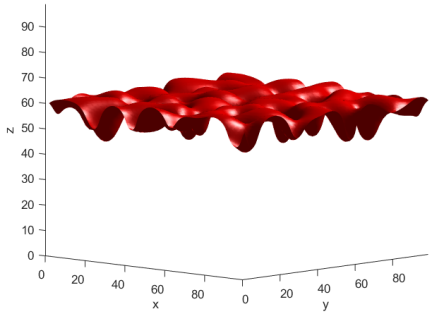

(b) The isosurface $\phi = 1/2$ at $t = 100$. Grooves have formed at all parts of the interface, and there is no difference between x and y directions because uniaxial strain implies $\sigma_{xx} = \sigma_{yy} \neq 0$.

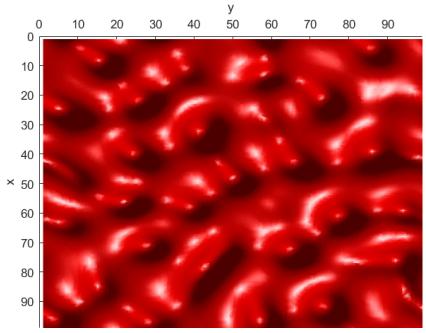

(c) The isosurface $\phi = 1/2$ at $t = 100$ from a birds eye view.

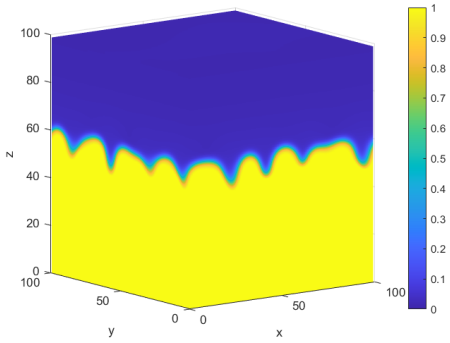

(d) The phase field at $t = 100$, showing the bulk of the phases $\phi = 1$ and $\phi = 0$ separated by an interface from a certain viewing angle.

Figure 3.21: Evolution of the phase field in 3d with parameters $Lx = Ly = Lz = 100$, $c = 8$, $\epsilon = \Delta x = 0.3$, and initial random profile under uniaxial strain. The best way to see the interface is to surface plot the isosurface $\phi = 1/2$, which is essentially the definition of it.

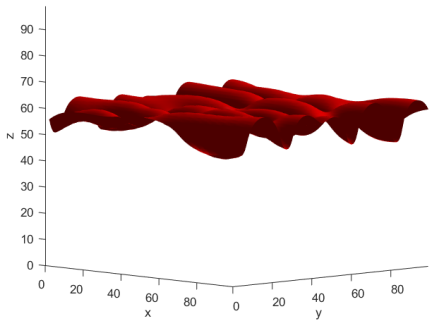

(a) The isosurface $\phi = 1/2$ at $t = 100$. Grooves have formed mostly along the y direction, because $\sigma_{yy} \neq 0$ whereas $\sigma_{xx} = \sigma_{zz} = 0$.

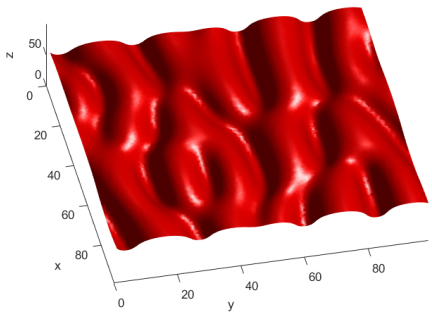

(b) The isosurface $\phi = 1/2$ at $t = 100$ from a birds eye view. It is a clearer view of the stripes.

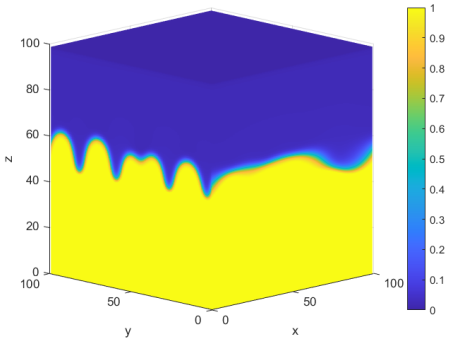

(c) The phase field at $t = 100$, showing the bulk of the phases $\phi = 1$ and $\phi = 0$ separated by an interface from a certain viewing angle. Here the difference between x and y directions is very clear.

Figure 3.22: Evolution of the phase field in 3d with parameters $Lx = Ly = Lz = 100$, $c = 8$, $\epsilon = \Delta x = 0.3$, and initial random profile under uniaxial stress along the y direction. The best way to see the interface is to surface plot the isosurface $\phi = 1/2$, which is essentially the definition of it. Stripes form because of the asymmetry between x and y directions.

Chapter 4

Conclusion and Future Work

The advantage phase field modeling has in solving interfacial problems is mainly its simple numerical implementation, due to the fact that the boundary separating different phases is tracked implicitly by the phase field itself. Another advantage is the ability to couple it to other fields, such as temperature and elastic fields, to incorporate their influence on interface dynamics. Both of these advantages are highlighted in modeling Grinfeld instability by using a non-conserved phase field coupled to an elastic field.

Naturally, such a model is attractive when thinking about biological systems, which have a clear boundary separating them from the outside world, and the dynamics of which is greatly influenced by elasticity. However, a direct application is not adequate for two reasons: 1) A conserved phase field must be used for living beings, and 2) The instability can not grow indefinitely, it has to be limited. We solve these inconveniences by first using conservative dynamics, and second by limiting the growth of the instability through a time-dependent external stress. This is accomplished via a parameter $c(t)$ that decreases with time. We study a linearly decreasing function and power-law decay, and conclude that the latter is much better for mimicking the out-of-plane buckling observed in Placozoa. To be precise, when the parameter depends on time as $c = 6(t+1)^{-0.2}$, an initial random surface will grow and coarsen. Eventually, there will be only one groove that keeps growing, but very slowly. For short enough time intervals, it resembles the steady state observed in videos of Placozoa. We also explore how different parameters in these functions account for different time and length scales. Lastly, we extend the model to 3 dimensions, but unfortunately, due to time limitations, it was not possible to study time-dependent behavior.

The work done in this thesis sets the stage for exciting future explorations, which can happen on two fronts: computational/theoretical and experimental.

On the first front, it is possible to completely model the creature as a whole (not just a part of it) in 3D, which might be quite challenging. One challenge is the fact that the equilibrium configuration for a phase field model in 3D is a sphere, whereas the equilibrium configuration for the creature is a disk. This

can be resolved by introducing an anisotropic surface tension that makes the disk energetically favorable over the sphere. Another challenge is how to introduce the elastic terms along with their appropriate boundary conditions. Doing this is not trivial, but one possible route is to introduce a random velocity field that models the motion of the creature, and couple the elastic field to it, causing stress to be generated if the creature moves in a certain way. Needless to say, many more challenges may appear along the way. Finally, another possibility is to use phase field crystal modeling, which incorporates elasticity more naturally. However, this model is used more for solids, and it is not adequate in modeling amorphous creatures. This also might be solved by introducing a velocity field explicitly.

On the second front, more experiments need to be done with this creature, and better videos must be produced. For complete modeling, one needs to experimentally obtain the elastic moduli of the creature, and a side-view rather than a birds eye view will immensely help in clearly defining some characteristics of this buckling, such as how long it lasts and how large is the out-of-plane deformation.

Appendix A

Numerical details

The equations are solved using the finite differences method. The time derivative is approximated as

$$\frac{\partial \phi}{\partial t} = \frac{\phi(t + \Delta t) - \phi(t)}{\Delta t}, \tag{A.1}$$

and the simplest way to approximate the Laplacian is to use the 5-point stencil

$$\nabla^2 \phi = \frac{\phi(i+1,j) + \phi(i-1,j) + \phi(i,j+1) + \phi(i,j-1) - 4\phi(i,j)}{\Delta x^2}. \tag{A.2}$$

However, this only includes nearest-neighbor terms, which makes the operator unstable when ϕ is varying quickly (unless a really small Δx is chosen). A better form of the Laplacian operator is given by the 9-point stencil that includes next nearest neighbors

$$\begin{aligned} \nabla^2 \phi = {} & 4[\phi(i+1,j) + \phi(i-1,j) + \phi(i,j+1) + \phi(i,j-1)] \\ & + \phi(i+1,j+1) + \phi(i+1,j-1) + \phi(i-1,j+1) + \phi(i-1,j-1) \\ & - 20\phi(i,j)/(6\Delta x^2). \end{aligned} \tag{A.3}$$

In order to check for optimal values for Δx and Δt, it is always a good idea to do a Von Neumann Stability analysis on the equations, which basically means analyzing the stability of fourier modes, $\phi = c(t)e^{ik_x x}e^{ek_y y}$ (which are eigenvectors of the Laplacian operator, with negative eigenvalues). Applying the above Laplacian gives

$$\begin{aligned} \nabla^2 \phi &= \frac{c(t)}{6\Delta x^2}\big[4(2cos(k_y \Delta x) + 2cos(k_x \Delta x)) \\ &\quad + 4cos(k_y \Delta x)cos(k_x \Delta x) - 20\big]e^{ik_x x}e^{ek_y y} \\ &= \frac{\lambda}{6\Delta x^2}\phi. \end{aligned} \tag{A.4}$$

This is used in the linearized form of equation 2.59

$$\frac{\phi(t + \Delta t) - \phi(t)}{\Delta t} = \beta \nabla^2(\phi - \epsilon^2 \nabla^2 \phi), \tag{A.5}$$

and the final result is:

$$c(t+\Delta t) = \left\{1 + \frac{\Delta t\lambda}{6\Delta x^2}\big[1 - \frac{\epsilon^2}{6\Delta x^2}\lambda\big]\right\}c(t). \tag{A.6}$$

This fourier mode is stable as long as the term in the curly brackets is less than 1 in magnitude. The worse case scenario is when $\lambda = -32$, which gives an upper bound on Δt

$$1 - \frac{32\Delta t}{6\Delta x^2}\big[1 - \frac{32\epsilon^2}{6\Delta x^2}\big] > -1, \tag{A.7}$$

$$\Delta t < \frac{72\Delta x^4}{32(6\Delta x^2 - 32\epsilon^2)}. \tag{A.8}$$

A similar equation can be obtained in 3D, using a 27-point stencil that is the simple extension of the 9-point stencil [21]. It should be noted that if the 5-point stencil was used instead of the 9-point one, then the upper bound on Δt would be significantly lower.

Besides the phase-field and its partial derivatives, there is one more term in the dynamical equation, which is the last term due to elasticity:

$$\frac{\partial\phi}{\partial t} = \beta\nabla^2\big[(1-\phi)(2\phi - 4\phi^2) - \epsilon'^2\nabla^2\phi + cg'(\phi)h(\phi)\big], \tag{A.9}$$

where $h(\phi)$ is obtained from the strain tensor and its trace

$$h(\phi) = [f_1 + \sum_{ij}(u_{ij} + \frac{\delta_{ij}}{d}g)^2]. \tag{A.10}$$

In turn, f_1 and u_{ij} are obtained for a given phase field ϕ by imposing mechanical equilibrium, which results in the following equations:

$$\nabla^2 u_{ij} = -\frac{\epsilon}{\kappa}\nabla_i\nabla_j g, \tag{A.11}$$

$$\nabla^2 f_1 = -\frac{2}{\kappa}\sum_{ij}\frac{\partial}{\partial x_i}\frac{\partial}{\partial x_j}\left[g(u_{ij} + \frac{\delta_{ij}}{d}\frac{\epsilon}{\kappa}g)\right]. \tag{A.12}$$

These are Poisson equations which can be solved using the relaxation method. Therefore, for each time step, 4 Poisson equations need to be solved (3 for the strain tensor because it's symmetric, and one for f_1) in 2D, or 7 in 3D.

Firstly, to better understand the relaxation method and why it works, consider a simple 1D equation

$$\frac{\partial^2 u(x)}{\partial x^2} = s(x), \tag{A.13}$$

where $s(x)$ is some function, sometimes called a source function. The first step is to write it as a finite difference equation (FDE):

$$u(i+1) + u(i-1) - 2u(i) = \Delta x^2 s(i). \tag{A.14}$$

Writing it this way actually changes the initial differential equation to a set of linear equations, one equation for each lattice point i. Such a set can be written in matrix form

$$\boldsymbol{Au} = \boldsymbol{S}. \tag{A.15}$$

Therefore, the solution can be obtained by any method used to solve similar matrix equations, like LU decomposition [22]. We use an iterative approach (Jacobi Method), the reasons for which will become clear later. This method is based on rewriting equation A.14 in the following way:

$$u(i) = \frac{u(i+1) + u(i-1) - \Delta x^2 s(i)}{2}, \tag{A.16}$$

which basically says that the value of the function u at a given point i is given by a combination of its nearest neighbors and the source function. The idea behind the Jacobi Method is to start with an initial guess for the solution $u(x)$, and use equation A.16 iteratively to converge to the real solution. let the index k denote the k_{th} iteration. The value of the function at each lattice point i at the next iteration is given by:

$$u^{k+1}(i) = \frac{u^k(i+1) + u^k(i-1) - \Delta x^2 s(i)}{2}. \tag{A.17}$$

To see if this will converge to the real solution, rewrite the above equation in matrix form:

$$\boldsymbol{u^{k+1}} = \boldsymbol{Bu^k} + \boldsymbol{c}, \tag{A.18}$$

with $\boldsymbol{B}$ being a tridiagonal matrix with diagonal elements zero and nearest off-diagonal elements 1/2:

$$\boldsymbol{B} = \begin{bmatrix} 0 & 1/2 & & & \\ 1/2 & 0 & 1/2 & & \\ & 1/2 & \ddots & \ddots & \\ & & \ddots & \ddots & 1/2 \\ & & & 1/2 & 0 \end{bmatrix}.$$

Suppose that the initial guess is the vector $\boldsymbol{u_0}$, and the actual answer is $\boldsymbol{u}$, which satisfies $\boldsymbol{u} = \boldsymbol{Bu} + \boldsymbol{c}$. The difference between the value at the k_{th} iteration and the real solution is given by:

$$\boldsymbol{u^k - u} = \boldsymbol{B(u^{k-1} - u)} = \boldsymbol{B^k(u_0 - u)}. \tag{A.19}$$

Now $\boldsymbol{B}$ is a matrix which can be diagonalized. Denote its eigenvalues as λ and eigenvectors as $\boldsymbol{v}$. The difference between the first guess and the actual solution can be expanded in this basis:

$$\boldsymbol{u_0 - u} = \alpha_1 \boldsymbol{v_1} + \alpha_2 \boldsymbol{v_2} + \cdots + \alpha_n \boldsymbol{v_n}. \tag{A.20}$$

Inserting this in equation A.19, and using the fact that $\boldsymbol{B^{k+1}v_i} = \lambda_i \boldsymbol{v_i}$ results in:

$$\boldsymbol{u^k - u} = \alpha_1 \lambda_1^k \boldsymbol{v_1} + \alpha_2 \lambda_2^k \boldsymbol{v_2} + \cdots + \alpha_n \lambda_n^k \boldsymbol{v_n}. \tag{A.21}$$

Therefore, as $k \to \infty$, the difference between the k_{th} iteration and the actual result, a.k.a. the error, will go to zero only if:

$$|\lambda_i| < 1 \quad \text{for all} \quad i = 1, 2, \ldots, n. \tag{A.22}$$

This argument can be easily generalized to higher dimensions. It should be noted that first, the source function is irrelevant when considering convergence of the solution, and second, for the Poisson equation, the matrix $\boldsymbol{B}$ does satisfy the criterion for convergence. Lastly, the efficiency of this method is based upon how good of a guess is the initial vector.

The final ingredient for the Jacobi method is to decide when to stop iterating, because numerically it is impossible to take the limit $k \to \infty$ to obtain the exact solution. This decision is made based on a small parameter δ that dictates error tolerance. The iteration is stopped if, for every i, the next iteration does not change the value of the function by more than this tolerance:

$$\left|u^{k+1}(i) - u^k(i)\right| \leq \delta \quad \text{for all } i. \tag{A.23}$$

For all the simulations, the error tolerance was set at $\delta = 10^{-6}$.

Going back to the equations for the strain tensor, first A.11 must be solved, because the solutions form the source function for A.12. Consider A.11 for $i = j = 1$, which we denote as the x-component (ignore the prefactors for simplicity):

$$\nabla^2 u_{xx} = -\frac{\partial^2 g}{\partial x^2}. \tag{A.24}$$

The source function $\frac{\partial^2 g}{\partial x^2}$ is calculated beforehand numerically. Denote it by g_{xx} and write the equation as an FDE (with the nine-point stencil):

$$\begin{aligned}\nabla^2 u_{xx} &= 4[u_{xx}(i+1,j) + u_{xx}(i-1,j) + u_{xx}(i,j+1) + u_{xx}(i,j-1)] \\ &\quad + u_{xx}(i+1,j+1) + u_{xx}(i+1,j-1) + u_{xx}(i-1,j+1) + u_{xx}(i-1,j-1) \\ &\quad - 20u_{xx}(i,j)/(6\Delta x^2) \\ &\quad = -g_{xx}(i,j).\end{aligned} \tag{A.25}$$

This is also a system of equations which can be solved using the Jacobi method. At the start of a simulation, the random initial guess for u_{xx} is set as a matrix of zeros. However, afterwards, the solution obtained after relaxation is used as the initial guess for the relaxation at the next time step. This is a good initial guess because after one time step the phase field does not change drastically, so neither

will the strain tensor, and this is what makes the Jacobi method very efficient for this problem. After the complete strain tensor is obtained, the source function for f_1 can be calculated and equation A.12 can be solved similarly.

Finally, the boundary conditions need to be specified such that the phase field is uniaxially stressed along the horizontal direction in the solid phase, and there is no stress in the liquid phase. This can be achieved by the following conditions for a simulation box of size L (these will be written without prefactors because eventually all of them will be factored out and absorbed in the parameter c):

$$u_{yy}(x, y = 0, L) = -g(x, y = 0, L), \tag{A.26}$$

$$u_{xx}(x, y = 0, L) = 0, \tag{A.27}$$

$$u_{xy}(x, y = 0, L) = 0, \tag{A.28}$$

$$f_1(x, y = 0, L) = g^2(\phi(x, y = 0, L)). \tag{A.29}$$

Equation 2.50 can be used to show that these conditions imply $\sigma_{xx} = 2g^2$, and $\sigma_{yy} = \sigma_{xy} = 0$ at the vertical boundaries. Along with these, periodic boundary conditions are imposed along the horizontal direction.

Appendix B

Surface Profile and Height-Height Correlation

To obtain all the results, one needs to extract the profile of the interface as a function of position from a given phase-field $\phi(x, y)$. This can be done by first obtaining the function $\phi(x, y)(1 - \phi(x, y))$, which will be 0 in the bulk of each phase ($\phi = 1$ and $\phi = 0$), and a maximum at the interface defined by $\phi = 1/2$. For a given phase-field, this function is shown in figure $B.1$

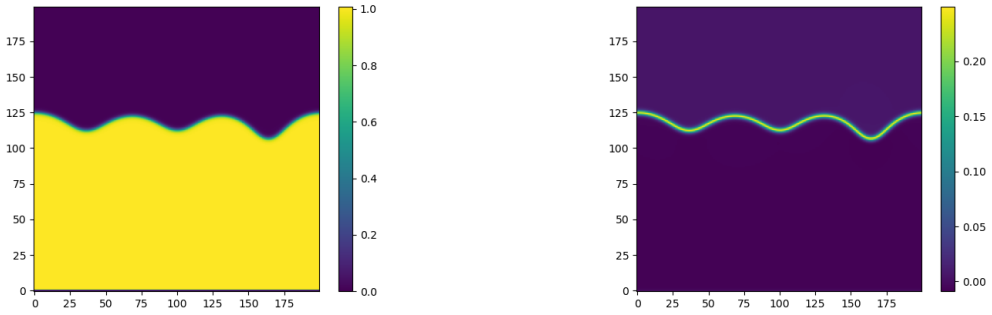

(a) A certain phase-field with $\phi = 0, 1$ corresponding to the different phases, separated by a smooth interface.

(b) The function $\phi(1-\phi)$, which is 0 in the bulk of both phases and maximum at the interface defined by $\phi = 1/2$.

Figure B.1: The first step for extracting the profile of the interface for a given phase field.

Now, all that's required is to loop over the horizontal axis (x), and store the value on the vertical axis (y_i) that correspond to the maximum of $\phi(x_i, y)$, for a given x_i. For the above phase field, this results in the surface profile shown in figure B.2

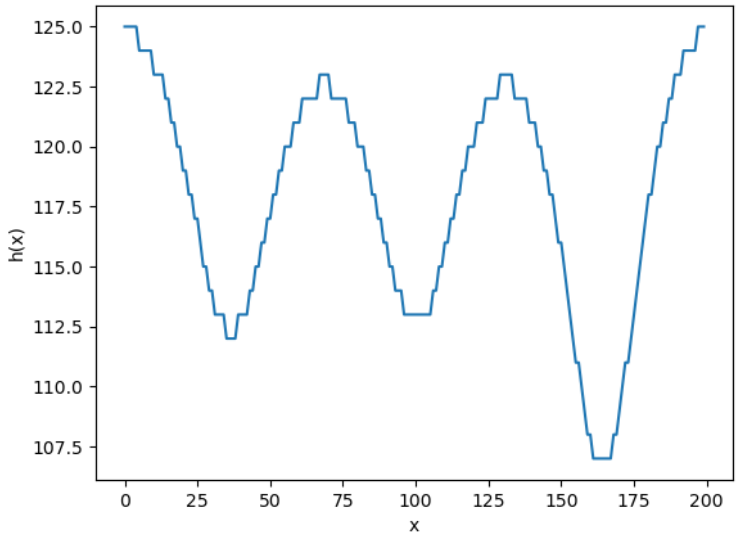

Figure B.2: The profile obtained by the above method.

Once the profile is obtained, the height-height correlation function can be calculated from the definition

$$H(x') = \langle [h(x+x') - h(x)]^2 \rangle_x. \tag{B.1}$$

For a given distance x' (here ranging from 0 to 200), one loops over the profile and averages the difference in heights $h(x+x') - h(x)$ over all possible values of x (ranging from 0 to 199 for a total of 200 points). The Fourier transform of this function can be easily obtained using a Fast Fourier Transform (FFT). The zero order amplitude in Fourier space corresponds to the average value of the function in real space, and since that is irrelevant, it is removed from the function before doing the FFT.

Bibliography

[1] A. M. Meirmanov, *The Stefan Problem*, vol. 3. Walter de Gruyter, 2011.

[2] N. Provatas and K. Elder, *Phase-field methods in materials science and engineering*. John Wiley & Sons, 2011.

[3] P. C. Hohenberg and B. I. Halperin, "Theory of dynamic critical phenomena," *Reviews of Modern Physics*, vol. 49, no. 3, p. 435, 1977.

[4] H. Gomez and K. G. van der Zee, "Computational phase-field modeling," *Encyclopedia of Computational Mechanics Second Edition*, pp. 1–35, 2018.

[5] T. Takaki, "Phase-field modeling and simulations of dendrite growth," *ISIJ international*, vol. 54, no. 2, pp. 437–444, 2014.

[6] J. Müller and M. Grant, "Model of surface instabilities induced by stress," *Physical Review Letters*, vol. 82, no. 8, p. 1736, 1999.

[7] K. Kassner, C. Misbah, J. Müller, J. Kappey, and P. Kohlert, "Phase-field modeling of stress-induced instabilities," *Physical Review E*, vol. 63, no. 3, p. 036117, 2001.

[8] K. Elder, M. Grant, N. Provatas, and J. Kosterlitz, "Sharp interface limits of phase-field models," *Physical Review E*, vol. 64, no. 2, p. 021604, 2001.

[9] S. Najem and M. Grant, "Phase-field model for collective cell migration," *Physical Review E*, vol. 93, no. 5, p. 052405, 2016.

[10] S. Najem and M. Grant, "The chaser and the chased: a phase-field model of an immune response," *Soft matter*, vol. 10, no. 48, pp. 9715–9720, 2014.

[11] S. Najem and M. Grant, "Coupling actin dynamics to phase-field in modeling neural growth," *Soft matter*, vol. 11, no. 22, pp. 4476–4480, 2015.

[12] C. L. Smith, N. Pivovarova, and T. S. Reese, "Coordinated feeding behavior in trichoplax, an animal without synapses," *PloS one*, vol. 10, no. 9, p. e0136098, 2015.

[13] G. Lebon, D. Jou, and J. Casas-Vázquez, *Understanding non-equilibrium thermodynamics*, vol. 295. Springer, 2008.

[14] R. W. Balluffi, S. M. Allen, and W. C. Carter, *Kinetics of materials*. John Wiley & Sons, 2005.

[15] L. D. Landau, "On the theory of phase transitions," *Ukr. J. Phys.*, vol. 11, pp. 19–32, 1937.

[16] J. W. Cahn and J. E. Hilliard, "Free energy of a nonuniform system. i. interfacial free energy," *The Journal of chemical physics*, vol. 28, no. 2, pp. 258–267, 1958.

[17] M. Kardar, *Statistical physics of fields*. Cambridge University Press, 2007.

[18] A. J. M. Spencer, *Continuum mechanics*. Courier Corporation, 2004.

[19] I. Cantat, K. Kassner, C. Misbah, and H. Müller-Krumbhaar, "Directional solidification under stress," *Physical Review E*, vol. 58, no. 5, p. 6027, 1998.

[20] A. Onuki, "Long-range interactions through elastic fields in phase-separating solids," *Journal of the Physical Society of Japan*, vol. 58, no. 9, pp. 3069–3072, 1989.

[21] R. C. O'Reilly and J. M. Beck, "A family of large-stencil discrete laplacian approximations in three dimensions," *Int. J. Numer. Methods Eng*, pp. 1–16, 2006.

[22] M. Newman, *Computational physics*. CreateSpace Independent Publ., 2013.